GENIORS

Research and Innovation Action (RIA)

This project has received funding from the European Union's Horizon 2020 research and innovation programme under grant agreement No 755171.

Start date : 2017-06-01 Duration : 48 Months
http://geniors.eu/

Innovative dissolution routes for highly plutonium doped (U,Pu)O2 and (U,Pu,MA)O2 samples

Authors : Dr. Gilles LETURCQ (CEA)

GENIORS - Contract Number: 755171

Project officer: Roger Garbil

Document title	Innovative dissolution routes for highly plutonium doped (U,Pu)O2 and (U,Pu,MA)O2 samples
Author(s)	Dr. Gilles LETURCQ
Number of pages	51
Document type	Deliverable
Work Package	WP4
Document number	D4.2
Issued by	CEA
Date of completion	2021-05-31 14:07:00
Dissemination level	Public

Summary

The use of the Micro Series mill, made it possible through different stress modes applied to the sample to reduce the size of the reference CeO2 particles down to the nanometer scale. This reduction in particle size results, in a first approach, by an increase in the specific surface from 0.7 to 29.5 m².g-1. Dissolution tests ([HNO3] = 8.5 M and T = 95 ° C) of the reference sample after grinding demonstrate a significant increase in dissolution kinetics. The modification of certain grinding parameters made it possible to maximize the first, faster dissolution rate. The simultaneous grinding / dissolution tests on CeO2 under mild chemical attack conditions ([HNO3] = 0.5 M and T = 50 ° C) led after 3 h to a dissolution rate of 33% much higher than 0.5% achieved with simple grinding (at 6 h of dissolution).

Approval

Date	By
2021-05-31 14:08:50	Mr. Nicolas DACHEUX (CEA)
2021-06-01 09:50:54	Mr. Andreas GEIST (KIT)
2021-06-01 10:53:08	Mr. Stéphane BOURG (CEA)

CONTENT

This project has received funding from the EURATOM research and training programme 2017-2021 under grant agreement No 755171. The content of this deliverable reflects only the author's view. The European Commission is not responsible for any use that may be made of the information it contains.

This project has received funding from the EURATOM research and training programme 2017-2021 under grant agreement No 755171. The content of this deliverable reflects only the author's view. The European Commission is not responsible for any use that may be made of the information it contains.

INTRODUCTION

It is planned to develop generation IV, fast reactors (FR) for the multi-recycling of plutonium. This fuel is composed of depleted uranium and plutonium at 20-30 wt%. Recycling processes should take into account the increase in Pu content in future spent nuclear fuels (1% UOX, <10% LWR MOX and up to 30% FR fuel) [1]. If spent UOx fuel is easily dissolved in nitric acid, dissolution of spent MOX fuel is more difficult due to the presence of Pu-rich clusters. Indeed $U_{1-x}Pu_xO_2$ phases with x higher than 0.3 almost stays undissolved after 6h in concentrated nitric acid [2]. Therefore, considering spent FR MOX treatment, simple nitric dissolution would end up with Pu rich residues that would have to be recovered to prevent any criticality accident. Complementary treatments for these dissolution residues are under development in order to keep a Pu recovery yield of 99.9% as it is for UOX fuels [3]. These Pu based residues being strongly resistant to corrosion in conventional nitric acid media, many studies were devoted to optimize chemical conditions of the attack conditions. Improvement of dissolution kinetics require an hardening of these chemical conditions by modifying the main dissolution parameters (acidity [4; 5], temperature [6], addition of complexing agent [7; 8]). One option is to use nitric and hydrofluoric acid mixtures at boiling temperature under reflux [8]. However, the kinetics of reaction is very slow for high temperature treated oxides with low specific surface area (less than $1 m^2.g^{-1}$) and solutions are highly corrosive which raises reactor corrosion issues. These conditions induce some problems for the following steps of PUREX process. Another option, currently used in La Hague, ORANO plant for dissolving non-compliant PuO_2, requires a low content of electroregenerated Ag(II). This ion allows the oxidation of Pu(IV) to Pu(VI) enhancing dissolution kinetics [9].

Another possibility to improve oxides dissolution kinetics is the enhancement of solid reactivity by an increase of specific surface area and the formation of energetically reactive sites [10- 12] like oxygen vacancies and linear defects. Some studies in literature report that higher dissolution kinetics correspond to materials having the smallest crystallite sizes and thus the highest specific surface areas [13]. The role of preferentially attacked sites with high surface energy on the initial dissolution rate is also mentioned in the literature for ceramic materials [14] . Mechanical activation, usually done by high-energy milling, is considered as an alternative route to current processes. Milling show significant acceleration of dissolution processes due to the generation of structural defects, being high-energy reaction sites and catalyze dissolution reactions [15 - 17].

CeO_2 is frequently used as a surrogate for plutonium dioxide, their similitudes are detailed and compared in next paragraph. Both materials are resistant to hydrometallurgical dissolution processes. Therefore, a solution for improving the dissolution of ceria would probably also be useful for dissolving the oxides rich in Pu. Several studies deal with ceria dissolution modelling. The effect of microstructural properties of CeO_2 on its dissolution in nitric acid 8.5M at 95°C was modeled only with two variables: crystallite size (Tc in nm) and specific surface area (SSA in $m^2.g^{-1}$), r being the dissolution kinetics in %dissolved.min^{-1} [18]:

$$r = k \times Tc^{-1} \times SSA^{0.33} \qquad \text{Eq. 1}$$

This project has received funding from the EURATOM research and training programme 2017-2021 under grant agreement No 755171. The content of this deliverable reflects only the author's view. The European Commission is not responsible for any use that may be made of the information it contains.

Another model was established as a function of several defects identified in ceramic oxides in case of dissolutions in nitric acid medium at 90°C [19].

$$C_{Ce} = \frac{SSA}{SSA_0}\left[\alpha A_3\left(1 - e^{-b_3 t}\right) + (1 - \alpha)A_4\left(1 - e^{-b_4 t}\right)\right] \quad \text{Eq. 2}$$

Where C_{Ce} is the concentration of Ce, SSA ($m^2.g^{-1}$) is the measured specific surface area (after dissolution in the case of CeO_{2-x}), SSA_0 is a reference specific surface area of 1 $m^2.g^{-1}$, α is the fraction of Ce^{3+} (representing the oxygen vacancy content determined by XPS), A_3 and A_4 correspond to the solubility limits of Ce^{3+} and Ce^{4+} respectively, and b_3 and b_4 are the rate constants for Ce^{3+} and Ce^{4+}.

The highest CeO_2 dissolution rate was observed for the sample exhibiting greater amounts of high-energy surface sites, intrinsic defects and oxygen vacancies. Dissolution of these oxygen vacancy sites in CeO_{2-x} is greatly increased due to the presence of Ce^{3+}. The greater solubility of Ce^{3+} influenced the dissolution rate compared to Ce^{4+} in CeO_2 like those calcined at high temperatures. Moreover, oxygen vacancy ratio change the lattice volume and constraint the crystalline structure. Dissolution improves by stress relaxation induce by lattice strain. Introduction of trivalent element inside the ceria structure leads to both the creation of oxygen vacancies and to an increase strain in lattice. Such addition creates oxygen vacancies and constrains the crystal lattice resulting in a higher dissolution rate. Some articles deal with the incorporation of trivalent lanthanides (La, Nd, Sm, Gd, Dy, Er, Yb) to create oxygen vacancies and modify solid properties in order to promote dissolution [20 ; 21]. It was shown that samples doped with trivalent elements are more efficiently dissolved. Others authors have optimized chemical media, with sonochemical method, involving platinum nanoparticle deposit on the cerium oxide and the addition of ascorbic acid to initiate a reductive dissolution [22].

The present work deals with the development of a milling and dissolution combining process to enhance dissolution kinetics of ceria, the latest being used as a surrogate of Pu-rich oxides. In the first chapter, synthesis and characterization of ceria samples used for this study are exposed. The milling device is also presented. In the second chapter, the effect of grinding on CeO_2's structure and microstructure is exposed. The influence of these modifications on dissolution is investigated. To understand these effects, kinetics and mechanism of cerium oxide dissolution are examined by comparing activated samples with un-grinded ones exhibiting equivalent microstructural properties. Then, an optimization study was carried out on milling parameters in order to enhance dissolution kinetics prior to apply them on milling and dissolution combining process within the last chapter.

EXPERIMENTAL DETAILS

CeO_2 SURROGATE OF PuO_2 AND BY EXTENSION SURROGATE OF HIGHLY PLUTONIUM DOPED-$(U,Pu)O_2$ OR $(U,Pu,AM)O_2$

CeO_2 is used as a surrogate for PuO_2 since both oxides crystallize in the same fluorite-type structure (FCC, Fm-3m, PDF cards 03-065-2975 for CeO_2 and 00-051-0798 for PuO_2) with equivalent ionic radius (Ce^{4+}=0.97 Å and Pu^{4+}=0.96 Å).

With similar free energies of dissolution (ΔrG_{Ce}^0 = 40 $kJ.mol^{-1}$ for cerium oxide and ΔrG_{Pu}^0 = 41 $kJ.mol^{-1}$ for plutonium oxide [23], the dissolution of these oxides is not thermodynamically favorable. Ziouane *et al.*[18], studied the dissolution of PuO_2 and CeO_2 as a function of structural parameters (initial micro strain, crystallite

This project has received funding from the EURATOM research and training programme 2017-2021 under grant agreement No 755171. The content of this deliverable reflects only the author's view. The European Commission is not responsible for any use that may be made of the information it contains.

size) and microstructural (specific surface area, particle size, morphology) depending on the conditions of production (synthesis route, calcination temperature) and conditions of dissolution (acidity, temperature). Like cerium dioxide, plutonium dioxide is refractory to dissolution in a nitric medium. Aggressive dissolution conditions must be used to significantly improve kinetics. The dissolution of these two oxides follows the same model. This model depends on the nature of the oxide, the structural and microstructural parameters and environmental conditions. By maintaining the attack conditions (at 8.5 M HNO_3 and 95°C) and these parameters constant, the authors demonstrated that the kinetic constant of CeO_2 is only 3 times greater than that of PuO_2. This validates the use of CeO_2 to simulate the behavior of PuO_2 on dissolution. Reducing dissolution can also be applied to both oxides in order to enhance dissolution rates **[24; 25]**.

It was also shown that for plutonium content over 30% dissolution of mixed actinide oxides is similar to dissolution of PuO_2 making ceria also a surrogate for such phases.

CERIA SYNTHESES

High purity (>99.9%) Sigma-Aldrich commercial reagents were used for this study. Two different routes were performed in order to synthetize CeO_2 powder with different microstructural proprieties.

In a first step, two CeO_2 batches were obtained by thermal conversion of oxalate precursors precipitated in excess of oxalic acid from cerium nitrate solutions. The oxalic conversion is usually reported to synthetize actinide oxides **[26[27]**. Cerium nitrate hexahydrate was dissolved in water. The cerium precipitate was obtained by mixing this solution containing Ce(III) with oxalic acid as complexing agent solution. Concentrations of these solutions were fixed in order to reach in the precipitator a final concentration of nitric acid equal to 1 $mol.L^{-1}$ and an oxalic excess of 0.20 $mol.L^{-1}$. Oxalic precipitation of trivalent cerium leads to an oxalate with $Ce_2(C_2O_4)_3$, $10H_2O$ formula **[28 - 30]**. The solid obtained by this route presents a monoclinic structure and crystallized in the form of platelet agglomerates. The precipitate was filtered and rinsed with deionized water before being air-dried. To obtain oxides with different microstructural properties, this precursor was split onto two batches before being calcined under air atmosphere at 1200°C and 600°C respectively with a heating rate of 5°C.min^{-1} and the final temperature maintained for 2 hours before cooling down to room temperature. The aim of the use of different calcination temperatures is the obtaining of two oxides with different microstructural properties.

In a second step, a batch of ceria was obtained using Nitrate Poly-acrylate Gel (NPG) method in presence of Poly(ethylene glycol)-block-poly(propylene glycol)-block-poly(ethylene glycol) (P123). Cerium nitrate ($Ce(NO_3)_3$) was dissolved in nitric acid. P123 was dissolved in the cerium solution. Then, this solution was added to acrylic acid (AA) and N, N'-methylene bis (acrylamide) (MBAM). The resulting homogeneous solution was heated up to 100°C. 25 µL of hydrogen peroxide and ascorbic acid were quickly incorporated to initiate the complete polymerization of the solution to form a gel. This gel was finally dried at 150°C to form a xerogel, which was converted in oxide through an oxidative calcination at 600°C in air for 2 h. During this treatment, the total oxidation of all residual carbon compounds takes place, leading to oxide synthesis **[31]**. This NPG method was used since it is known to for the development of a process for the synthesis of actinide or lanthanide oxide on a smaller scale. The advantage of this method is that it allows a low production of liquid effluents, thus increasing the compactness of the process.

This project has received funding from the EURATOM research and training programme 2017-2021 under grant agreement No 755171. The content of this deliverable reflects only the author's view. The European Commission is not responsible for any use that may be made of the information it contains.

CHARACTERIZATION OF THE SOLID

METHODS

X-Ray Diffraction analyses of the synthesized powders were performed using a D8 Bruker Advance diffractometer equipped with a linear Lynx-eye detector using Cu-Kα radiation (λ = 1.5418 Å). The powder patterns were recorded with an angular range from 20° to 120° in 2 theta, with steps of 0.02° and a counting time of 0.5 s per step. The micro-strains and average crystallite sizes were calculated using the Hadler Wagner Langford method as implemented in the JANA 2006 software [32].

The specific surface area of the different oxides was determined with a Micromeritics TriStar II Plus Version 2.02. Nitrogen adsorption was performed at 77 K after an overnight treatment under vacuum at 130°C to ensure their complete outgassing. Such settings and device allow a limit of quantification of 1 $m^2.g^{-1}$ and a statistical error of 5%. For values lower than 5 $m^2.g^{-1}$ the nitrogen is replaced by krypton to minimize the measurement uncertainty to 0.05 $m^2.g^{-1}$.

The size distribution of the particles is measured before but also after grinding using a Malvern Master Sizer 2000 particle size analyzer. The powders were suspended in a flask and then treated in an ultrasonic bath for 10 min to break the agglomerates. Part of this solution is added to the closed water circuit until the obscurator exceeds a limit value of 13%. The suspension is analyzed three times with an acquisition time of 12 seconds, resulting in a reliable size distribution. For particle sizes smaller than 0.1 µm, dynamic light scattering (DLS) complements laser granulometry. Measurements were performed by the Zetasizer Nano ZS in static mode. 1 mL of suspension wass placed under ultrasound for 5 min and then filtered through a 0.2 µm syringe filter and supplemented with Synthron B03 used as dispersant.

Microstructure analyses of the all powders were also performed using a Scanning Electron Microscope (SEM). The samples were deposited on carbon adhesive tape with additional gold deposit of a few angstroms for CeO2 treated at 1200°C. A Hirox SH 4000M scanning electron microscope was used to record images with an acceleration voltage of 30 kV under high vacuum conditions.

The nanoscale characterization of milled oxide was carried out with High-Resolution Transmission Electron Microscopy (HR-TEM) after deposition of oxide suspension on carbon coated copper grids. The oxide suspension was previously prepared in water and sonicated in an ultrasonic bath for 8 min. CeO_2 samples were studied by STEM and EELS by using a Titan Themis (Thermo Fisher) microscope operating at 200 kV.

RESULTS ON RAW CERIA SAMPLES

As already pointed out, two routes were used to synthesize the oxides. The first one, the oxalic precipitation, allow to synthesize ceria powder with typical agglomerated platelets shapes. SEM observations shown in Figure 1 allow to determine individual platelets median sizes of 15 µm by 8 µm and surface charge effects led to agglomerated pre-sintered particles of a hundred of micrometer width. Several crystallites compose CeO_2

This project has received funding from the EURATOM research and training programme 2017-2021 under grant agreement No 755171. The content of this deliverable reflects only the author's view. The European Commission is not responsible for any use that may be made of the information it contains.

platelets. In literature, some authors referenced that platelet morphology is preserved during calcination, but calcination temperature changes crystallite size. Similar platelet morphologies of CeO_2 particles can be observed from SEM micrographs after 600°C and 1200°C (**Figure 1**). XRD patterns, also in **Figure 1**, confirm a CeO_2 structure with fluorite-type (PDF card 03-065-2975) for all oxides and highlight the difference of Full-Width Half-Maximum (FWHM) between oxides treated at 1200°C and 600°C. The increase of FWHM at lower calcination temperature gives evidence of a reduction of the crystallite size (i.e. the coherent domain size). In accordance with this, Table 1 summarizes refinement results of coherent domain size and indicates the size increase with temperature. CeO_2 treated at 1200°C was afterward defined as the reference of this study, since it possess the largest size, the smallest micro-strain, due to the highest calcination temperature that confer to this oxide the hardest to dissolve character [33].

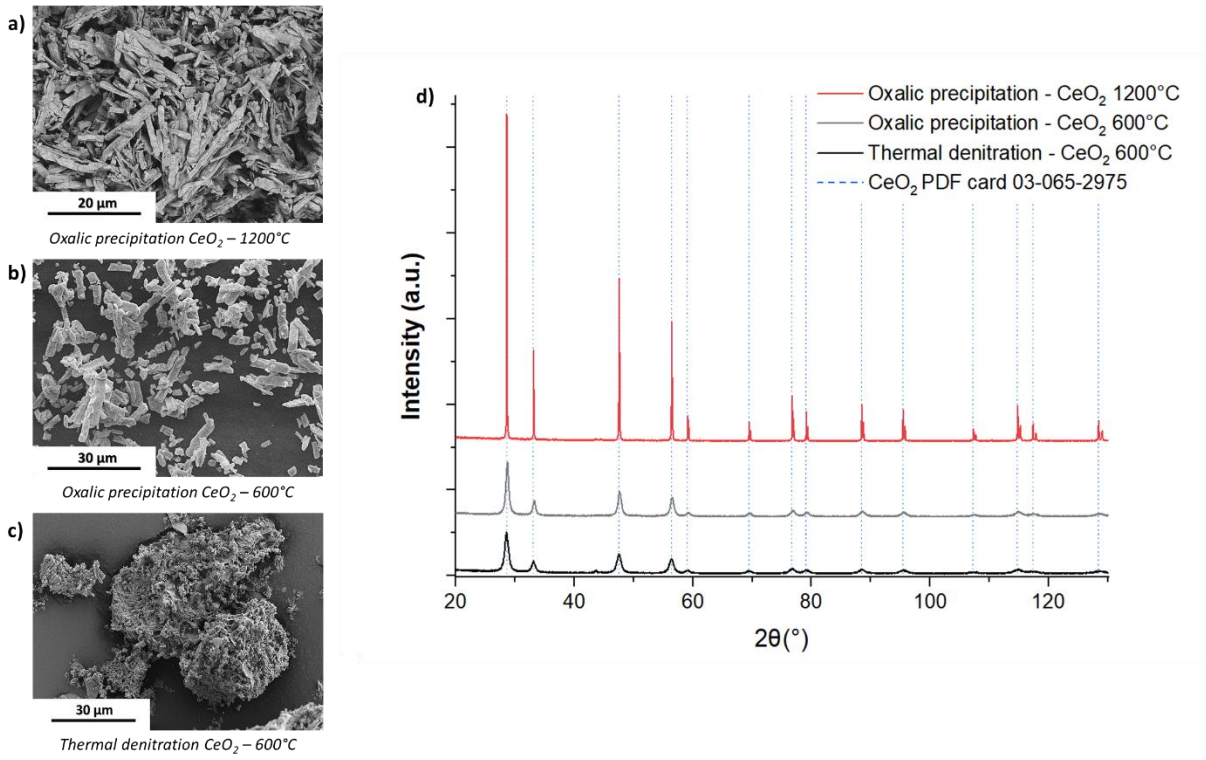

Figure 1 :SEM images of a) cerium oxide obtained by oxalic precipitation and heat treated at 1200°C and b) 600°C for 2 hours and c) obtained by second route, advanced thermal denitration and heat treated at 600°C for 2h. XRD of respectively oxides, all corresponded CeO_2 structure (PDF 03-065-2975).

The second route, advanced thermal denitration, allows to synthesize CeO_2 powder batch (Figure 1 d)) with a different morphology, i.e composed of agglomerated nanometric particles. Extracted information from XRD (Table 1) lead to conclude this oxide batch has a small coherent domain size, equivalent to the one of the oxide obtained by oxalic precipitation and treated at 600°C. Also, these two oxides have similar specific surface area and micro-strain ratio.

This project has received funding from the EURATOM research and training programme 2017-2021 under grant agreement No 755171. The content of this deliverable reflects only the author's view. The European Commission is not responsible for any use that may be made of the information it contains.

Table 1: Specific Surface Area ($m^2.g^{-1}$), size of crystallites (nm) and micro-strain (%) calculated by Hadler Wagner Langford method from XRD of initial oxides

	SSA ($m^2.g^{-1}$)	Size (nm)	Strain (%)
Oxalic precipitation - CeO_2 1200°C	0.7	121	6.5×10^{-4}
Oxalic precipitation - CeO_2 600°C	29.8	12	1.1×10^{-2}
Thermal denittration - CeO_2 600°C	30.8	9	1.4×10^{-2}

MILLING PROCEDURE

The grinding device used in this study is a NETZCH micro-serie (**Figure 2**) equipped with a ZETA grinding system consisting in the activation of grinding beads taking place within the agitator shaft composed of peg, disk or smooth-shaped agitating elements. Powder flow circulates continuously through the grinding chamber to reach a separation system. Grinding chamber and beads are composed of zirconia, this can resist to nitric acid. A 500mL tank is connected to the flow-through system allowing easy sampling.

Figure 2 : Principe of ZETA grinding and grinder Micro -Serie NETZSCH.

For the study of effects of milling on dissolution of ceria the milling parameters were first kept constant: a rotation speed of 4200 $tr.min^{-1}$ was used in the mechanical activation test of CeO_2. The reaction chamber was about 60 mL and balls used were 0.6 mm in diameter and represent 85% of total volume. The ceria mass to water volume ratio was 1:250 ($g.mL^{-1}$) for the milling operation. Ball-milling duration lasted for 60 min with a power input gross of 0.84 kW. The suspension containing water and ground cerium circulated thanks to a peristaltic pump with a flow rate of 110 $mL.min^{-1}$. Suspension was finally dried in a ventilated oven at 80°C to allow the recovery of the solid before characterizations.

These parameters were then changed to study their effects on dissolution kinetics, in order to optimize the milling and dissolution combining process, for this last part of the study water was replaced by nitric acid at the mentioned concentration.

This project has received funding from the EURATOM research and training programme 2017-2021 under grant agreement No 755171. The content of this deliverable reflects only the author's view. The European Commission is not responsible for any use that may be made of the information it contains.

DISSOLUTION PROCEDURE

Each dissolution test was performed in a 60 mL glass reactor shown in **Figure 3.** This dissolution reactor was designed specifically to contain 15 mL of nitric acid solution and to place the liquid at a sufficient height to be able to stir the solution using a magnetic bar. The top of the reactor has been designed with three small necks that allow the measurement and control of temperature, sampling and a wider central neck. The latter was connected to a refrigerating column, allowing the condensation of nitrous vapors likely to be released during the experiment. The end of the column was connected to a bubbler in which 2 M soda was placed. The soda trap ensured that if any nitrous vapors had not condensed they would have been completely trapped.

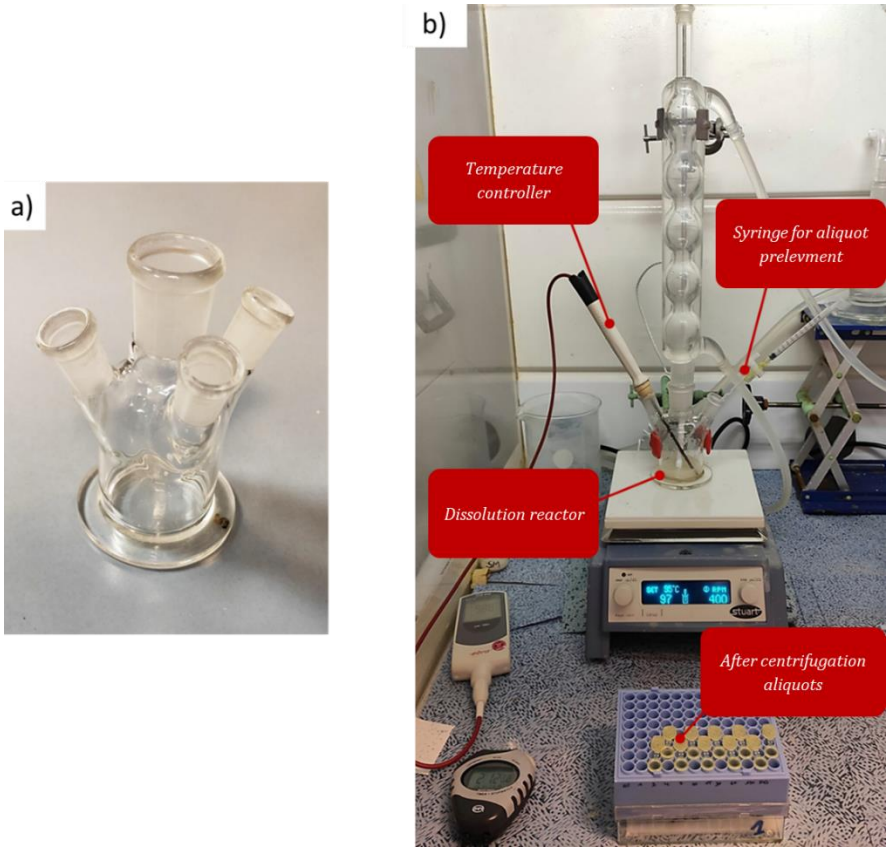

Figure 3 : a) dissolution reactor; b) full dissolution apparatus

Using a thermometer and a hot plate, the solution was thermostated to the temperature set for each experiment (50 ° C or 95 ° C) and stirred at 400 rpm. When the set temperature was reached, 300 mg of powder were added in the acid. The temporal monitoring of samples was punctuated by a stopwatch. From the very first moment, each 0.5 mL sample was placed in ice-cold water in order to stop any possible temperature-related dissolution phenomenon. After 10 min in a 4000-jet centrifuge, 0.4 mL is withdrawn using a syringe and then filtered (0.20 µm filter). Only 0.2 mL of this solution were then placed in a flask to then be diluted and analyzed analyzed using ICP-AES (for Inductively coupled plasma atomic emission spectroscopy) device (Horiba Jobin Yvon from Activa), after a dilution in order to keep a constant nitric acidity of 0.5 M and a cation concentration range from 0.1 to 10 ppm. External calibration curves were prepared with certified Ce and Zr

This project has received funding from the EURATOM research and training programme 2017-2021 under grant agreement No 755171. The content of this deliverable reflects only the author's view. The European Commission is not responsible for any use that may be made of the information it contains.

standard solutions of 1000 ppm (SCP Science). The error on each value depends on the law of uncertainty propagation, which considers dilution uncertainties, measurement errors, calibration and the device error. It can be expressed by the square root of the sum of the squares of the uncertainties. Uncertainties on mass of powder, volume of aliquot, dilution and ICP-AES measurements were taken into account. Dissolution progress is given as cerium dissolved percentage (%).

EFFECT OF MECHANICAL ACTIVATION BY HIGH ENERGY MILLING ON STRUCTURAL AND MICROSTRUCTURAL PROPERTIES OF CERIA AND CONSEQUENCE ON ITS DISSOLUTION KINETICS

STUCTUAL AND MICROSTRUCTURAL CHARACTERIZATIONS OF MILLED CERIA

The reference ceria (made by oxalic route and calcined at 1200°C) was ball-milled during 1 h in deionized water at the maximum shaft speed of 4200 tr.min^{-1} and then, dried during 2 days at 80°C.

SEM images on particles before and after 1 h milling indicate a change in oxide microstructure (**Figure 4**). Particles of reference CeO_2 heat-treated at 1200°C before milling correspond to a typical morphology of cerium oxide obtained by oxalic precipitation. The particle milling provokes the formation of porous agglomerates with a bigger specific surface area of 29.8 m².g^{-1} (0.7 m².g^{-1} for raw materials).

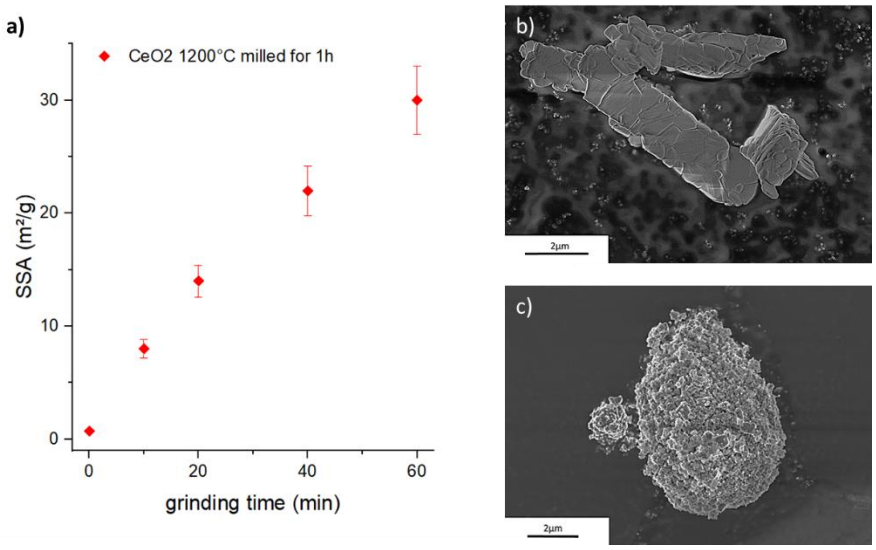

Figure 4 : a) Evolution of specific surface area during grinding CeO_2 heated at 1200°C and SEM image b) before and c) after 60min of grinding.

The particle size distribution of cerium oxide calcined at 1200 °C is mono-dispersed with an average particle size of 7 µm. The size distribution is between 0.8 and 100 µm. The particle size distribution corresponds to the contribution of both the width, the length and the thickness of the CeO_2 platelets obtained by oxalic precipitation. After one hour of grinding, two distinct populations are visible. The first is made up of

This project has received funding from the EURATOM research and training programme 2017-2021 under grant agreement No 755171. The content of this deliverable reflects only the author's view. The European Commission is not responsible for any use that may be made of the information it contains.

nanoparticles with a particle size of 8-10nm (zetameter) and a second larger in the order of a micrometer (particle size). The use of ultrasound to treat the solution reveals 3 populations on a particle size analyzer: 250 nm / 1-2 µm / 10-20 µm.

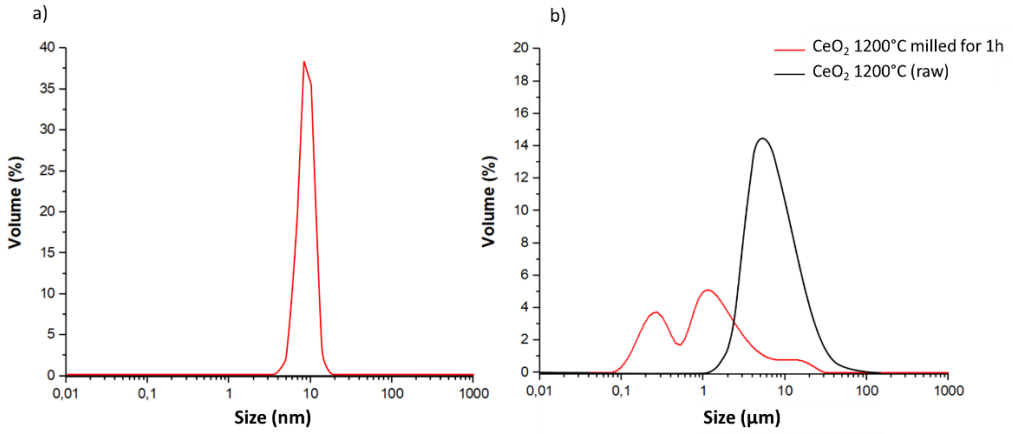

Figure 5 : a) Particle size and b) DLS analysis of CeO_2 before (black) and after grinding (red).

The X-ray diffraction (XRD) patterns of CeO_2 powders reference are characteristic of a monophasic fluorite-type structure, within Ce^{4+} is surrounded by eight equivalent O^{2-} ions forming the corner of a cube, with each O^{2-} coordinated to four Ce^{4+} ions. The diffractogram of CeO_2 ball-milled during 1h is also shown in XRD pattern of **Figure 6 a**). The observed pattern matches to a CeO_2 structure cubic fluorite-type. Upon modification, the peak positions (2θ) of the milled CeO_2 shifted toward a lower angle compared to raw CeO_2. The residual stress in the matrix generates a lattice expansion, leading to a shift in the peak positions. This peak shift to lower angles leads to an increase of cell lattice in agreement with Bragg Law and can be attributed to the formation of Ce^{3+} ions in CeO_2 nanoparticles. (Zhang et al., 2002), (ionic radius increase from 0.970 Å for Ce^{4+} to 1.143 Å for Ce^{3+}). As already reported, the oxidative state's change is accompanied by the loss of O^{2-} (1.380 Å) and oxygen vacancies' (1.164 Å) creation, affecting also the volume of CeO_{2-x}. (Lee et al., 2011; Spanier et al., 2001). In addition, as expected, milled oxide's diffraction pattern present higher Full-Width Half-Maximum (FWHM) than un-milled reference oxide, which involve the reduction of crystallite size in agreement with images (Deshpande et al., 2005).

This project has received funding from the EURATOM research and training programme 2017-2021 under grant agreement No 755171. The content of this deliverable reflects only the author's view. The European Commission is not responsible for any use that may be made of the information it contains.

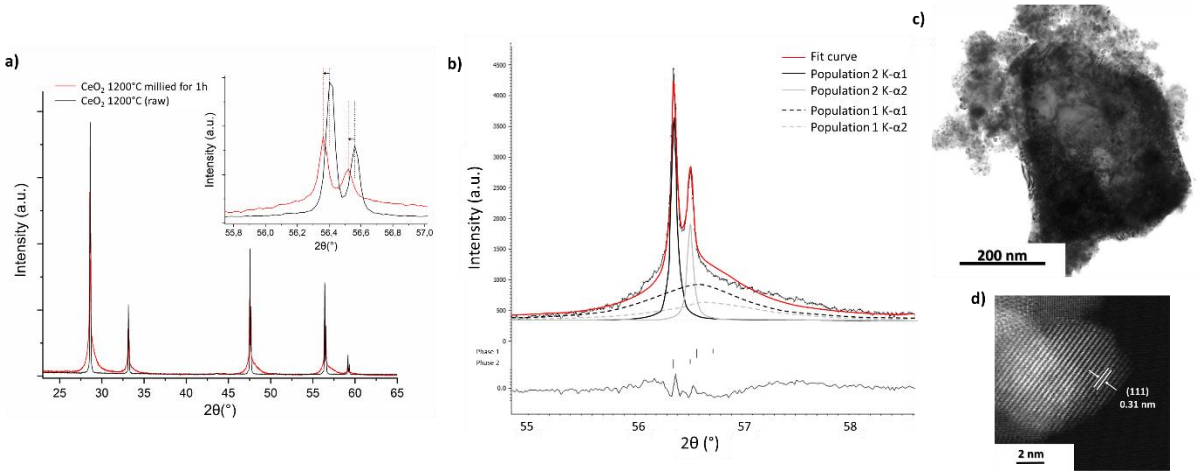

Figure 6 : a) XRD patterns of the CeO_2 before (red) and after (black) 1 hour of ball-milling. The inset displays the shifting and broadening of the peaks b)TEM images of CeO_2 before grinding with nanoparticles and grain and c) High-resolution scanning TEM images of nanoparticles showing sets of <111> planes and surfaces.

Table 2 : Specific Surface Area ($m^2.g^{-1}$), size of crystallites (nm), strain (%) and lattice parameter (Å) calculated by Fundamental parameters approach from XRD of initial oxides milled during 1h.

CeO_2 1200°C milled for 1h	SSA ($m^2.g^{-1}$)	Size (nm)	Strain (%)	Lattice parameter (Å)
Population 1	29.5	9	4.0×10^{-2}	5.3741
Population 2		150	2.1×10^{-3}	5.4101

(S)TEM images (**Figure 6 c) and d)**) and fitting of XRD peaks (**Figure 6 b and interpretation table 2**) reported the presence of a bimodal population after one hour of grinding, nanoparticles (Figure 6 c) and particles with similar size that initial crystallite before grinding. In accordance with this result, peaks deconvolution find the presence of two populations, nanoparticles and micronic particles with a highest micro-strain ratio than before grinding. A deeper study of these bigger grains revealed the presence of some defects (see after TEM study). The diffraction peaks fits show the presence of four curves, i.e $K_{\alpha1}$ and $K_{\alpha2}$ from two populations. The first, whose contribution is in full line, corresponds to population 2, the large grains. The second contribution, in dotted line, is attributed to population 1, nanosized ones. Table 1 allows to identify the information processed by these fits. Lattice parameter of population 2, particles with similar size that initial crystallite before grinding, correspond to a typical CeO_2 (5,4101 Å), but population 1, nanoparticles has a smaller parameter (5.3741 Å). Literatures **[34 - 36]** had demonstrated that the lattice parameter progressively decreases by Ce^{3+} inclusion with a smaller ion radius. Some authors had explained this shoulder at wide angles by the formation of nanohybrid **[37]** composed by Ce_2O_3/CeO_2. The CeO_2/Ce_2O_3 nanocomposite exhibited a similar diffraction pattern, but with the maxima shifted towards higher diffraction angles. It is clear that nanocomposites exhibited a greater number of Ce^{3+} ions, indicating a highly reducible nature of the nanostructures.

This project has received funding from the EURATOM research and training programme 2017-2021 under grant agreement No 755171. The content of this deliverable reflects only the author's view. The European Commission is not responsible for any use that may be made of the information it contains.

DEFECTS ON GRAIN

These defects corresponding at a dislocation area, as indicated by the appearance and disappearance of a line contrast at a specific orientation. The steps observed in **Figure 7a** (dark part on the left, the light area represents the void) reveal the sliding of the crystalline planes relative to each other. These types of atomic steps can only be observed in areas of shear that are finished as a free surface (as observed on **Figure 7**) or at grain joints. They are the manifestation of the movement, under the effect of the mechanical forces, of linear defects present in the crystal. The diffraction plane treatment by FFT shows the effect of introduction of an atomic half-plane inside the atomic planes at several places circled in red in **Figure 7**. Concentration of multiple dislocations can be identified on this strain zone. Dislocations, corresponding to the black lines present in the grains, are also observed on a larger scale. This contrast results from the decrease in the intensity of the transmitted beam linked to network distortions that locally modify the deviations from the Bragg angle near a defect. Two kinds of dislocation were identified, one extends through grain (**Figure 7b**) and the other (larger and shorter) accumulate at the point of initiation of the ball impact and abrade the surface (**Figure 7c)**.

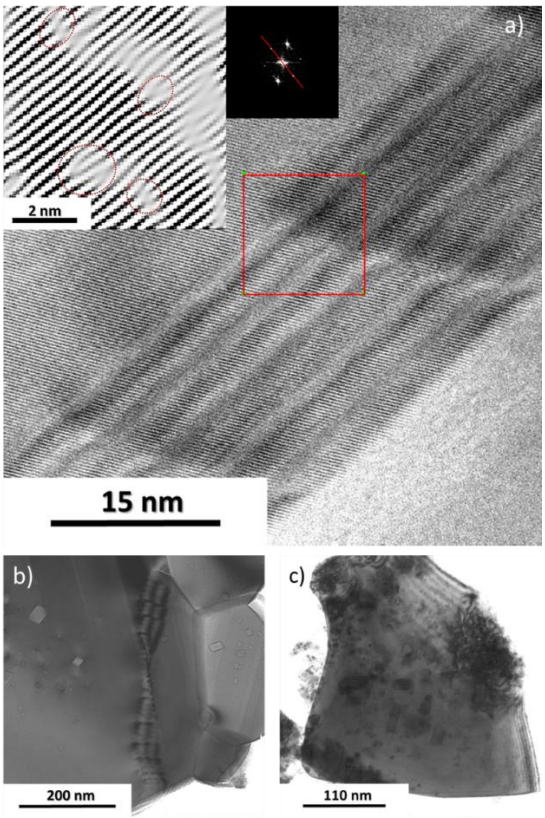

Figure 7 : a) A high-resolution TEM image of steps in massive grain surface of the ball-milled CeO_2 sample and by FFT highlights the presence of dislocations b) linear dislocation through the grain and strain field around c) accumulation of black arc reflecting the presence of dislocations.

This project has received funding from the EURATOM research and training programme 2017-2021 under grant agreement No 755171. The content of this deliverable reflects only the author's view. The European Commission is not responsible for any use that may be made of the information it contains.

CeO_2 NANOPARTICULES

Oxidation state of Ce in two nanoparticles of 7.8 nm and 4.3 nm, indicated by orange circles in HAADF-STEM image in **Figure 8 a**) were analyzed using EELS spectroscopy. **Figure 8 b**) demonstrates a local oxidation state map of Ce^{3+} (red) and Ce^{4+} (yellow). Local EELS spectrum corresponding area 1 to 4 are shown in **Figure 5 c)**. The $M_{4,5}$ edges on spectra are characteristic of transitions of 3d core electrons to unoccupied states of p- and f-like symmetry. The sharp M_5 and M_4 peaks (**Figure 8 c**)) arise from transitions from initial $3d^{10}4f^n$ state to the final $3d^94f^{n+1}$ state. The Ce^{4+} M_5 and M_4 edges (**Figure 8 c)1**) are separated by 18.1 eV and are composed of two main symmetrical maxima at 887.7 and 905.8 eV, and two broader and shorter maxima at 892.7 and 910.2 eV. The main M_5 and M_4 maxima of CeO_2 result from transitions from an atomic-like f^0 ground-state configuration. The Ce^{3+} $M_{4,5}$ edge shapes, intensities, and energies differ from those of Ce^{4+}. The Ce^{3+} (**Figure 8 c)**) M_5 edge displays a weak peak at 885.5 eV while the M_4 edge is more asymmetrical with a feature at 903.3 eV. In the zone 1, corresponding to the core of the particle, the spectra have a typical form of Ce^{4+}. However, at the particle surface (zone 3) the spectrum revealed Ce3+ feature. In the case of the nanoparticles, the Ce^{3+}/Ce^{4+} concentration decreases with the increase of particle size, as previously observed on similar samples, consistently with the reduced shell formation around an oxidized core **[38[39]**. In the small particle (4.6 nm in diameter indicated as zone 4), Ce^{4+} ions were totally reduced into Ce^{3+}. It is immediately apparent that the surface reduction shell is present over the whole particle surface. At its thinnest, the Ce^{3+} shell appears to extend over approximately 2 nm.

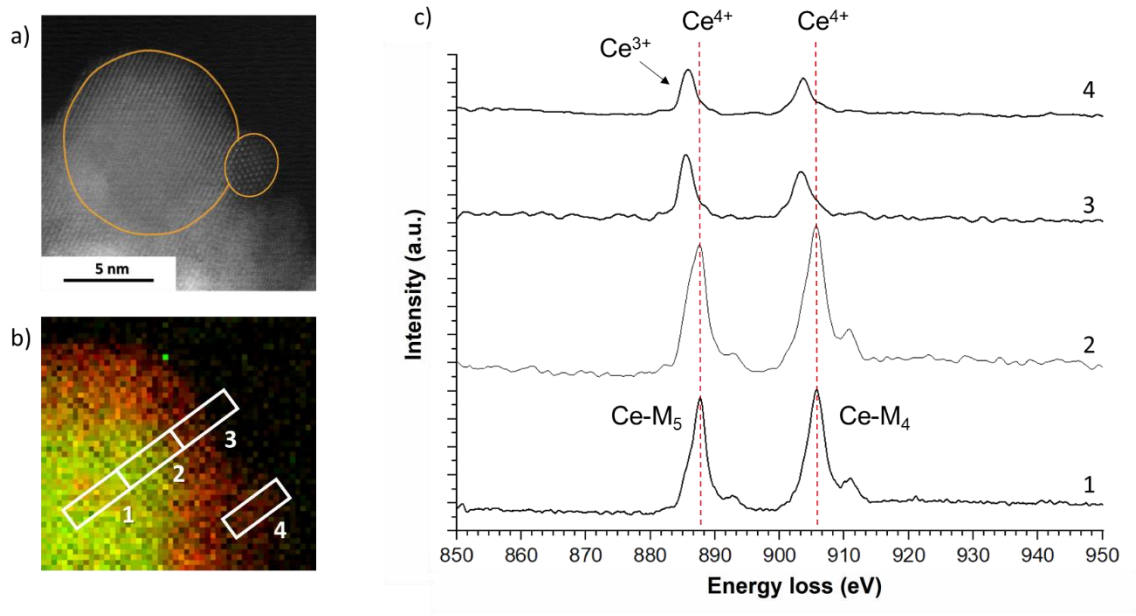

Figure 8 : a) STEM-HR of CeO2 NPs after one hour of ball-milling b) EELS maps of Ce^{3+} (red) and Ce^{4+} (green) oxidation state distribution c) Averaged Ce $M_{4,5}$ spectra from regions 1,2, 3 and 4 on the NPs EELS map.

This project has received funding from the EURATOM research and training programme 2017-2021 under grant agreement No 755171. The content of this deliverable reflects only the author's view. The European Commission is not responsible for any use that may be made of the information it contains.

FRAGMENTATION MECHANISM

Particle size and DLS analyzes (**Figure 3**) indicate that the category between 10 and 20 µm corresponding to chipped platelets does not represent a significant part by volume (a few%) and is therefore not very present. The second population, a few micrometers long, is more predominant and corresponds to detached or broken platelet grains. Finally, the last population consists of the largest nanoparticles.

The observation of the particle size's evolution during milling by Scanning Electron Microscope (**Figure 9 a,c,e**) allows to propose a fragmentation mechanism. Statistical analyses of recorded images confirm the progressive decrease in particle size related to grinding. First, these images show a rupture of the platelets characteristic of oxides obtained by oxalic precipitation. Each platelet is itself made up of crystallites with variable sizes. When these platelets fragment, grain boundary density decreases until fragments of equivalent size are obtained. After one hour of grinding, fragments have become, for the great majority, crystallites (that initially composed these fragments). Data acquisitions by TEM (**Figure 9 b,d,f**) confirm the presence of two mechanisms. For grinding times less than 40 min, holes with grain shape are observed, evidencing of the pullout of former grains. Beyond these 40 min, the majority of the grains have reduced in size. Comminuted solid consists of a few crystallites (platelet residue) with contrast black lines, attributed to dislocations.

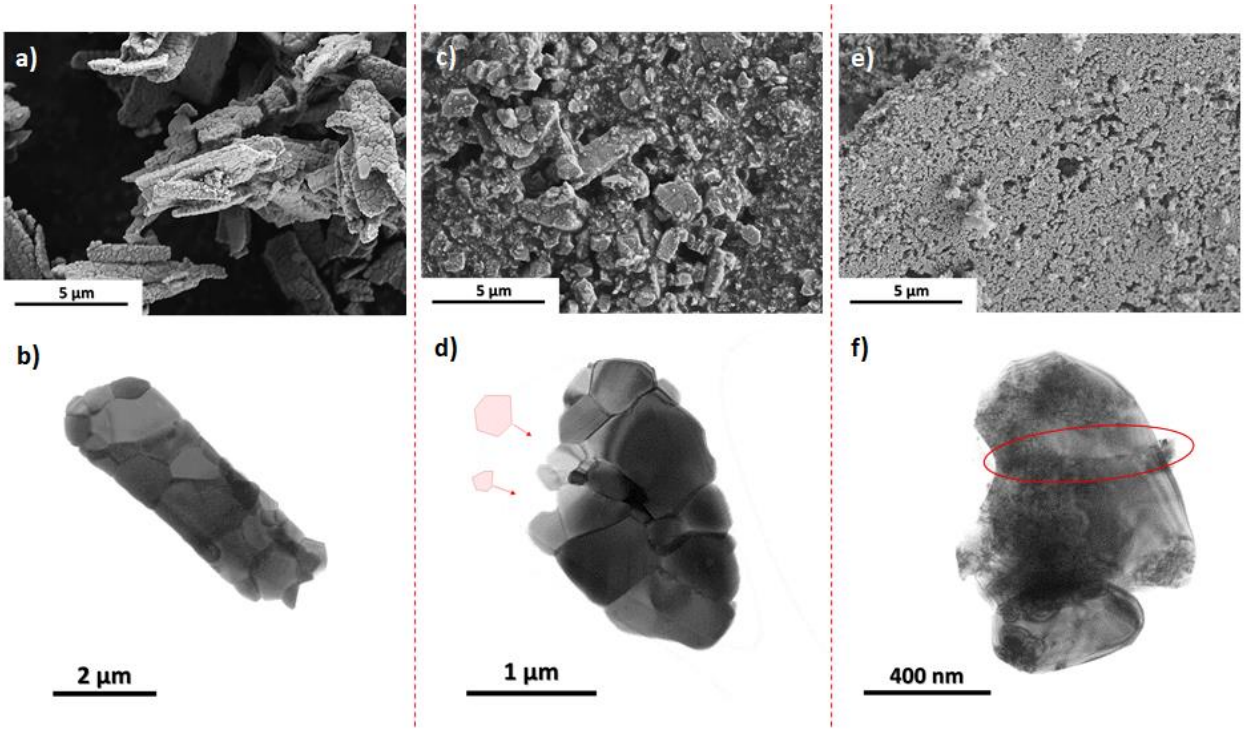

Figure 9 : Evolution of microstructure during milling at 0 min a) and b), 20 min c) and d) and 60 min d) and e) by SEM and STEM respectively.

DISSOLUTION

RESULTS

This project has received funding from the EURATOM research and training programme 2017-2021 under grant agreement No 755171. The content of this deliverable reflects only the author's view. The European Commission is not responsible for any use that may be made of the information it contains.

DISSOLUTION BEFORE/AFTER MILLING

In order to compare the influence of milling, dissolution tests of CeO_2 calcined at 1200°C were carried out in 8.5 M nitric acid at 95°C. It corresponds to the black curve in **Figure 10**. After 6 hours, the final dissolution rate is 0.1% of the initial oxide amount. Oxides calcined at high temperature has a strong refractory character to dissolution, in agreement with a low final dissolution rate and literature **[40]**. Kinetics is linear contrary to CeO_2 reference ball-milled during 1 hour. This same oxide calcined at 1200°C was ball-milled before being dissolved in the same conditions. The kinetics can be split into two regimes, the first one extends up to 30 min; at the end of this first step, dissolution rate was close to 20%. During the second step, it grows up to 36% after 6 hours. Kinetics of the first regime is fast; even if the second regime is slower than the first one, it is faster than the dissolution of the non-activated oxide. The grinding effect on the CeO_2 dissolution kinetics is far from negligible, as the dissolution rate increases by a factor of 360.

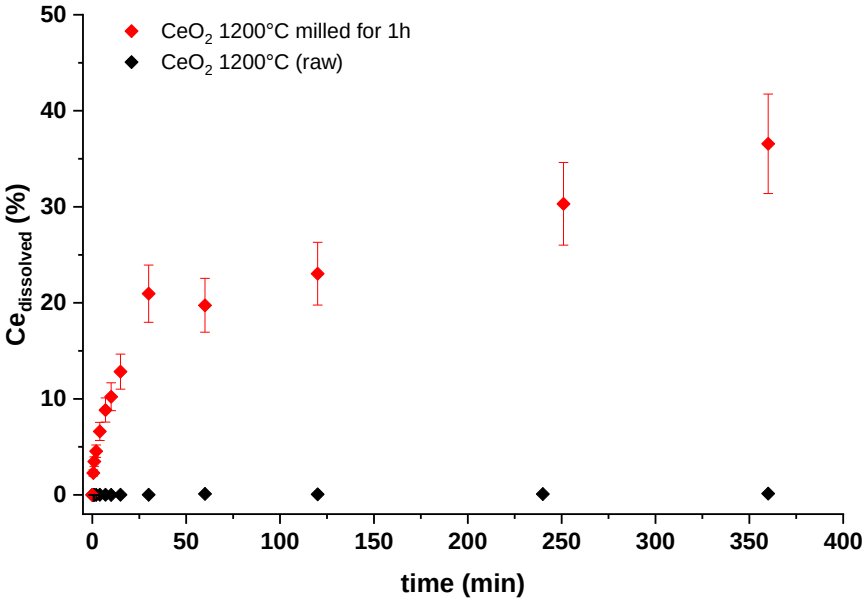

Figure 10 : Comparison between dissolution kinetics of CeO_2 calcined at 1200°C un-milled (black) and ball-milled CeO_2 (red).

KINETIC DISSOLUTION COMPARISON WITH SIMILAR CHARACTERISTICS MATERIALS

The ball-milled ceria dissolution (red curve) was compared to two other materials prepared at lower temperature**. Figure 11a** shows the comparison of dissolution kinetics of 1200°C ball-milled CeO_2 (the previous one) with the dissolution kinetics of un-milled CeO_2 obtained via the same oxalic route but calcined at 600°C. Both oxides exhibited similar specific surface area (29.5 $m^2.g^{-1}$ vs 29.8 $m^2.g^{-1}$). However, the un-milled oxide presents a final dissolution rate of only 13% and an almost linear kinetics unlike the ground sample. To illustrate if this kinetics difference is due to different morphologies (nanoparticle agglomerates vs rod massive

This project has received funding from the EURATOM research and training programme 2017-2021 under grant agreement No 755171. The content of this deliverable reflects only the author's view. The European Commission is not responsible for any use that may be made of the information it contains.

grains), dissolution kinetics for ball-milled CeO_2 at 1200°C and NPG CeO_2 have to be compared (Figure 11b). It shows that both samples exhibit the same specific surface area and also a morphology composed of nanoparticle agglomerates (**Figure 1**). Once again, dissolution of the un-milled sample only reaches 13% compared to the ball-milled one (36%) with an almost linear kinetics.

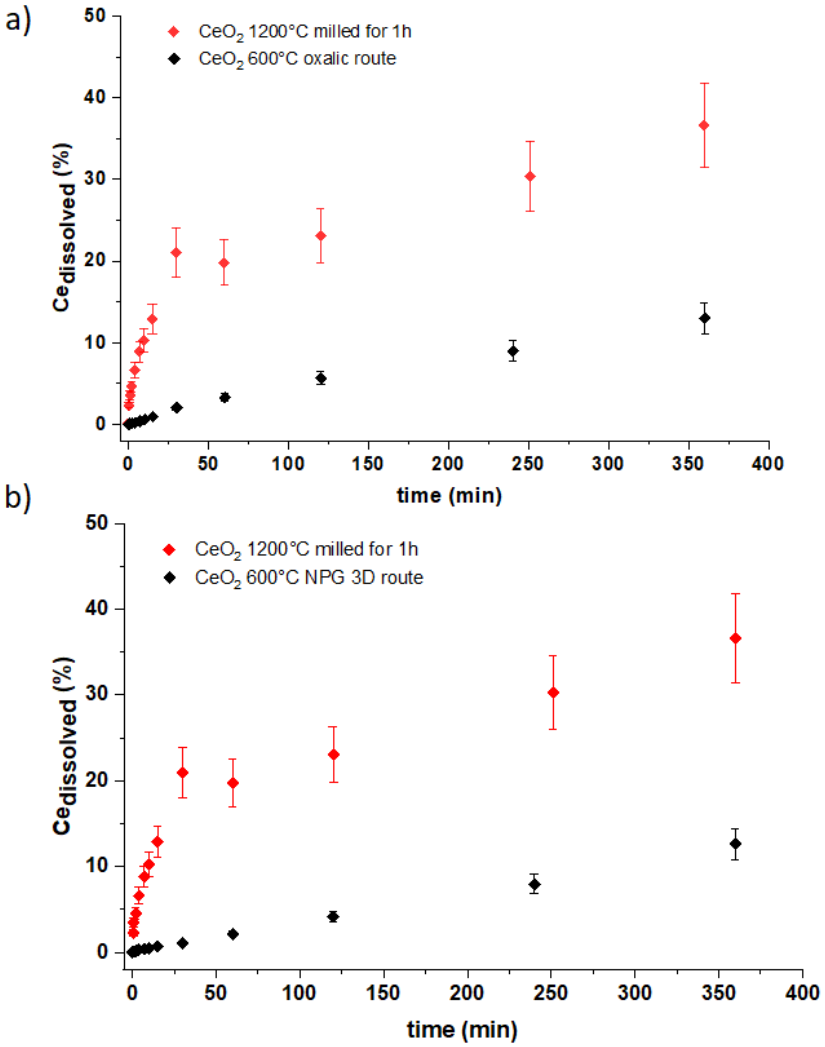

Figure 11 : Comparison between dissolution kinetics of CeO_2 calcined at 1200°C milled CeO_2 (red) and a) CeO_2 with same SSA and obtained via oxalic precipitation and treated at 600°C (black) and b) CeO_2 with same SSA and same morphology, obtained via NPG route and fired at 600°C (black).

DISCUSSION

CONTRIBUTION OF MILLING ON DISSOLUTION

The comparison of the dissolution kinetics between raw and grinded CeO_2 shows an increase in the dissolution rate by a factor of 360. The non-activated oxide has a 0.1% dissolution rate after 6h in HNO_3 95 °C while the

This project has received funding from the EURATOM research and training programme 2017-2021 under grant agreement No 755171. The content of this deliverable reflects only the author's view. The European Commission is not responsible for any use that may be made of the information it contains.

activated solid has been dissolved to an extend of 36%. The dissolution kinetics of milled oxide, can be describe like a kinetic in two stages unlike raw oxide. The first one is fast while the second one is slower as described on **Table 3.** The activated oxide kinetics, even for the slowest stage, is faster than the kinetics of the raw oxide.

Table 3 : Slope equation of CeO_2 calcined at 1200°C un-milled and ball-milled CeO_2 (two stages)

		Slope equation (%.min^{-1})
CeO_2 1200°C (raw)		$\%Ce_{dissolved} = 3.74\ 10^{-4}\ t + 5.79\ 10^{-3}$
CeO_2 1200°C milled for 1h	t < 30min	$\%Ce_{dissolved} = 6.42\ 10^{-1}\ t + 2.80$
	t > 30min	$\%Ce_{dissolved} = 5.60\ 10^{-2}\ t + 1.63\ 10^{1}$

Normalization to same SSA is not sufficient to explain this difference in kinetics as SSA grows only by a factor of 42, meaning dissolution kinetics acceleration cannot be only due to increase in specific surface area induce by size reduction. When the particle sizes decrease the dissolution kinetic increase **[40]**. Not everything can be explained by the size's reduction but this was the main factor. Over the grinding, the particle size decreased and the specific surface area increased to a final value of 29.8 m²/g after 1h.

Then, dissolution of the milled cerium oxide is compared to the dissolution of a cerium oxide also obtained by oxalic precipitation but calcined at a lower temperature in order to obtain equivalent specific surface area (29.8 m²/g) and coherent domain size (~12 nm). Despite these similar parameters for these two samples, dissolution kinetics of the un-milled oxide only reached 13% compared to the 36% observed on ball-milled oxide. However, despite both oxides were made using the same synthesis route, morphology of both samples is different due to the milling (Figure 4). The ball-milled oxide exhibits a microstructure made of nanoparticle's agglomerates and grains resulting from decohesion (**Figure 6**), while the 600°C annealed-raw oxide is made of aggregated platelets of about 20 µm size. One could, at first sight, assume that dissolution kinetics differences could result from such morphological changes.

To overcome the contribution of morphology, the dissolution of milled cerium oxide was compared to the one of a cerium oxide obtained by NPG route and calcined at 600°C. Both oxides have similar specific surface area (30.8 m²/g), similar crystallite sizes (~10 nm) and a comparable morphology (agglomerated nanoparticles). The dissolution kinetics are still different, the final dissolution rate achieved only 14% for NPG route compared to 36% for the ball-milled one. Therefore, grinding makes an additional contribution different from reduction of particle size and change in morphology. On top of the increase in terms of dissolved rates, dissolution kinetics of the ball-milled sample shows two regimes and not only one as observed on the two other samples.

The cerium oxide dissolution is thermodynamically impossible by the acid itself (ΔG_0=40 kJ.mol^{-1} **[25]**). It is only possible thanks to the complexation with the nitrate ions. According to the transition state theory and the collision theory to promote dissolution, it is necessary to provide sufficient energy called the activation energy, to reach the transition state. This transition state corresponds to the activated complex, as shown **Figure 12** (red line) that depicts a situation for dissolution of an unmilled ceria where the molar free energy of the dissolved and totally solvated species at the solvation plane is lower than in the oxide surface. As a dissolving species moves across the double layer there is an initial increase in chemical free energy, achieve to a peak as it

This project has received funding from the EURATOM research and training programme 2017-2021 under grant agreement No 755171. The content of this deliverable reflects only the author's view. The European Commission is not responsible for any use that may be made of the information it contains.

becomes a partially solvated activated complex, then decreasing as it approaches and becomes totally solvated at the solvation plane. The activation energy for dissolution is noted $\overrightarrow{\Delta G}_{CeO2}$ and the Ce^{4+} solution passage is $\overleftarrow{\Delta G}_{Ce^{4+}}$, where $\overrightarrow{\Delta G}_{CeO2} < \overleftarrow{\Delta G}_{Ce^{4+}}$.

To promote the dissolution beyond the surface effect, it is necessary to minimize the activation energy to reach the activated complex. In the case of ceria, the size reduction is accompanied by an oxidation state change. Analysis of the milled solid by XRD, STEM and EELS showed the presence of two populations. The nanoparticles exhibited a shell-core effect for diameter greater than 5nm, below this limit particle was completely reduced. The shell has a thickness of approximatively 2 nm and is composed of Ce^{3+}. Some authors had exploited this phenomenon, Ce^{3+} confers to the material some properties as ability to store and transport oxygen in catalysis. *Corkhill et al.* **[19]** demonstrated that sub stoichiometry of cerium oxide has a greater effect than the contribution of particle size on dissolution kinetics ($\overleftarrow{\Delta G}_{Ce^{3+}} < \overleftarrow{\Delta G}_{Ce^{4+}}$)**[36]**. By a charge compensation for oxygen vacancies, ionic radius between Ce^{3+} and Ce^{4+} decreases that contracts the fluorite cell. This contraction exhibits significant internal lattice strain, $\overrightarrow{\Delta G}_s$ that reduces the activation energy $\overrightarrow{\Delta G}_{CeO_{2-x}}$ (lower than $\overrightarrow{\Delta G}_{CeO2}$) in favor for the dissolution (green line **Figure 12**).

The activation energy can also be reduced by increasing the Gibbs free energy in the material surface. As observed, grinding has generated defects such as dislocation that change locally the plasticity on particle. Several studies **[14; [** 41**;[** 42**]** have already shown that when the dislocation's concentration increases, the dissolution is better. They have been modelized through equation 3 **[12]**, where :

$$\Delta G_d \approx (\rho_d M)\frac{b^2\mu}{4\pi}\ln\left(\frac{2(\rho_d)^{-1/2}}{b}\right) \qquad \text{(Equation 3)}$$

ρ_d : the dislocation density

M : the molar volume of the mineral

μ : the elastic shear modulus

b : the Burgers vector

The stored energy, $\overrightarrow{\Delta G}_d$ decreases the activation energy $\overrightarrow{\Delta G}_{CeO_{2+\varepsilon}}$ (red dotted line in **Figure 12)** compare to the activation energy of the unground oxide $\overrightarrow{\Delta G}_{CeO2}$.and also promotes the dissolution rate. Dislocations provide favorable reactive sites, by their resurgence on the surface and the creation of steps, for localized chemical attack. Other materials have shown higher dissolution rates with increasing density of dislocation.

In the present case, defects such as dislocations, strain and oxygen vacancies (Ce^{3+}) provoke the increase of initial activation energies in the solid. The activation energy required to reach the state of the activated complex is then lower than in the case of dissolution of non-activated CeO_2. All these contributions can be responsible for the increase of dissolution rate.

This project has received funding from the EURATOM research and training programme 2017-2021 under grant agreement No 755171. The content of this deliverable reflects only the author's view. The European Commission is not responsible for any use that may be made of the information it contains.

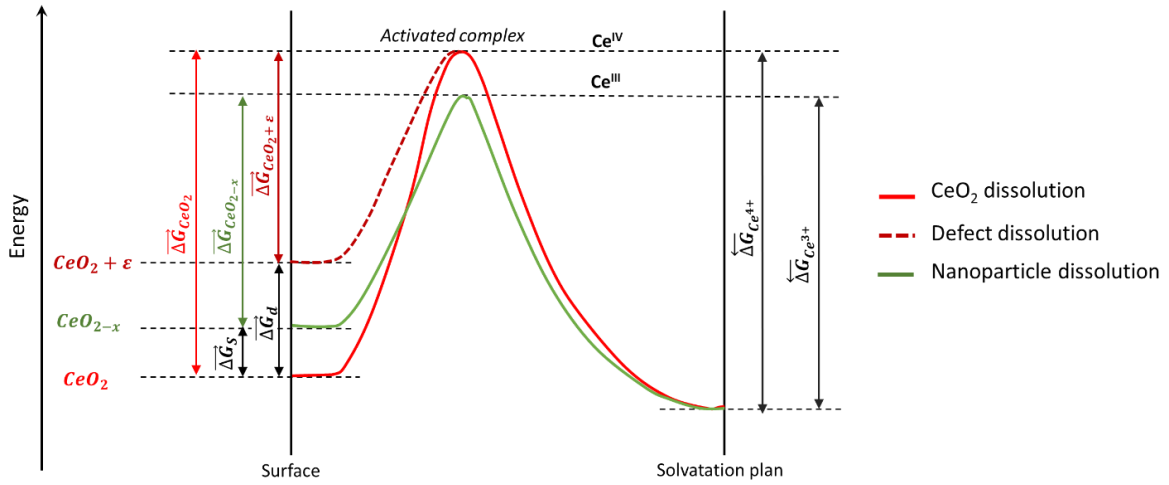

Figure 12 : Schematic diagram of the energy landscape of the solid after grinding. Three ways, in red the classic dissolution of CeO_2, in green the dissolution of CeO_2 containing Ce^{3+} and in red dotted line, the dissolution path of CeO_2 containing defects.

PHENOMENON IDENTIFICATION

The comparison of dissolution kinetics of CeO_2 milled for 1h, CeO_2 1200°C (raw) and CeO_2 600°C (from oxalic precipitation) with Ziouane *et al.*'s model (Equation 1) is shown on **Figure 13.** Note that this model was established from dissolution kinetics of oxides which have not been modified by any process such as grinding meaning it was built on ceria with no partial reduction. When the model is applied to cerium oxide obtained by oxalic precipitation and calcined at 600°C, the kinetics of dissolution measured correspond to the model ($3.36.10^{-2}$ %dissolved.min^{-1} vs $3.64.10^{-2}$ %dissolved.min^{-1} **Table 4**). Similarly, when applied to the reference material before milling (1200°C raw) (Tc = 120 nm and SBET = 0.7 m².g^{-1}) slope of experimental fit is of the same order of magnitude as the modelled figure (less than a factor 3 of difference that is on the model error bar: $3.74.10^{-4}$ % dissolved.min^{-1} vs $9.75.10^{-4}$ %dissolved.min^{-1}Table 4). Therefore, when applied to unground ceria Ziouane *et al.*'s model returns a good prediction.

At first sight, this model does not explain the dissolution of the ground material, as it does not predict the splits into two distinct regimes. In addition, the first regime, faster, does not correspond to any slopes of the model applied to the crystallite sizes determined by refinement of the X-ray diffractogram and specific surface area of the ground powder (**Table 4**). Reversely, for the model to match with dissolution fit of this first regime, the coherent domain size would have to be about 0.61 nm, which does not make physical sense. Therefore,

This project has received funding from the EURATOM research and training programme 2017-2021 under grant agreement No 755171. The content of this deliverable reflects only the author's view. The European Commission is not responsible for any use that may be made of the information it contains.

dissolution of CeO_2 at exact oxygen stoichiometry cannot be the phenomenon controlling this regime and Ce(+III) dissolution is more likely responsible to this faster dissolution regime.

The second regime is of the same order as that simulated from particles composed of crystallites of 7 nm long. This slope is also similar to the dissolution of CeO_2 obtained by oxalic precipitation and calcined at 600°C (5.60.10-2 %dissolved.min-1 vs 3.64.10-2 %dissolved.min-1 Table 6).

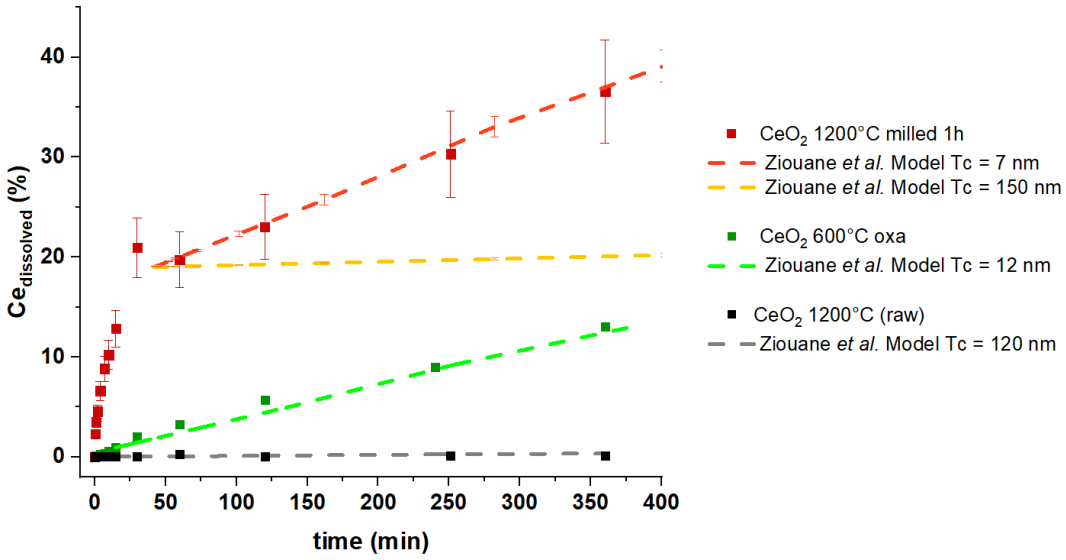

Figure 13 : dissolution kinetics of the reference oxide before (black dots) and after millng (red dots) compared to dissolution kinetics of CeO2 600°C oxa (green dots) and kinetics modeled by Ziouane et al. from crystallites (red curve) of 7 nm, of (orange curve) 150 nm, of (grey curve) 120 nm and of 12 nm (green curve) by XRD refinements.

Table 4: Fit equations of dissolution experimental kinetics (grey lines) of the reference oxide before and after milling, of the calcined oxide at 600°C and comparison with model with similar crystallite sizes and specific surface area.

	Tc (nm)	SSA ($m^2.g^{-1}$)		Slope equation (%.min^{-1})	R^2
CeO_2 1200°C milled for 1h	9	29.5	t < 30min	$\%Ce_{dissolved} = 6.42\ 10^{-1}\ t + 2.80$	0.954
	150		t > 30min	$\%Ce_{dissolved} = 5.60\ 10^{-2}\ t + 1.63\ 10^{1}$	0.999
Ziouane *et al.* Model Tc = 7nm	7	29.5		$\%Ce_{dissolved} = 5.60\ 10^{-2}\ t$	1
Ziouane *et al.* Model Tc = 150nm	150	29.5		$\%Ce_{dissolved} = 2.68\ 10^{-3}\ t$	1
CeO_2 600°C oxa	12	29.8		$\%Ce_{dissolved} = 3.64\ 10^{-2}\ t + 3.43\ 10^{-1}$	0.987
Ziouane *et al.* Model Tc = 12nm	12	29.8		$\%Ce_{dissolved} = 3.36\ 10^{-2}\ t$	1
CeO_2 1200°C raw	120	0.7		$\%Ce_{dissolved} = 3.74\ 10^{-4}\ t + 5.79\ 10^{-3}$	0.995
Ziouane *et al.* Model Tc = 120nm	120	0.7		$\%Ce_{dissolved} = 9.75\ 10^{-4}\ t$	1

This project has received funding from the EURATOM research and training programme 2017-2021 under grant agreement No 755171. The content of this deliverable reflects only the author's view. The European Commission is not responsible for any use that may be made of the information it contains.

For CeO_2 600°C oxa, the particles with a platelet form have an actual size with in the order of a micrometer but with a size of the coherent domains of 12 nm. The second regime of dissolution of the milled oxide is very close to the dissolution of such type of sample (platelet residues not having reached the nanometric scale but whose crystallites have been reduced to around 10nm). However, the milled solid consists of two populations composed of partially or totally reduced nanoparticles and residues of micron platelets with average crystallites size of 150 nm. If the coherent domains of the particles of the reference oxide milled for 1 h are 150 nm, i.e. the same size as those of the unground sample (gray curve **Figure 13**), the dissolution kinetics should have been equivalent and therefore very low (orange right **Figure 13**). However, as Table 6 shows, these kinetics are not in the same order of magnitude.

To explain the match of the kinetics of the second regime with dissolution of a material with smaller coherent domains, the solid have to correspond to grains containing dislocations. Well, as illustrated in **Figure 7b**, the ground particle exhibits such smaller crystallites. The one shown in this figure is divided into two by a dislocation and form two distinct smaller coherent domains.

STUDY OF EFFECTS OF MILLING PARAMETERS ON MICROSTRUCTURE EVOLUTIONS AND IMPACT ON DISSOLUTION KINETICS

Beyond the fundamental study of the impact of high energy milling on the microstructural changes and the understanding of the dissolution enhancement mechanism, a multiparametric study of milling was carried out in order to define the optimal parameters for the milling-dissolution coupling process to be implemented.

THE MILLING DURATION

The influence of the milling duration was studied in order to determine the limits of the milling then dissolution process. Therefore, the reference cerium oxide was ground with a maximum miller stirring speed of 4200 rpm^{-1} for a flow rate and a suspension concentration of 175 rpm^{-1} and 4.67 $g.L^{-1}$ respectively. Only the milling duration was changed for each of these five samples, ranging from 0 to 120 min. The dissolution conditions are identical for each of the tests, i.e. the temperature is maintained at 95 ° C in $[HNO_3]$ = 8.5 M. Each of the kinetics is represented on **Figure 14**.

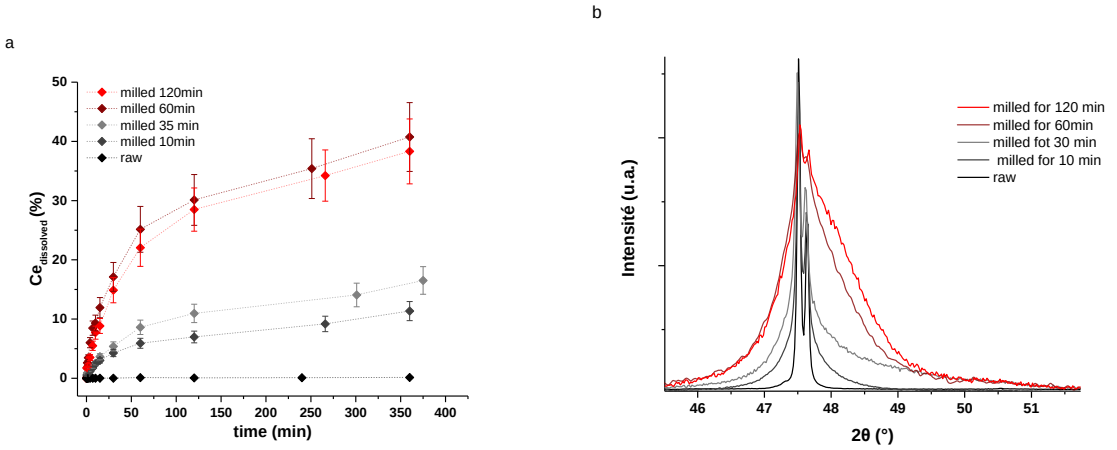

Figure 14 : a) kinetics rates of dissolution of raw and milled ceria for different milling duration times ([suspension]=4.67 $g.L^{-1}$;Vstirring =4200 rpm; Vpump=175 rpm) b) changes in X-ray diffraction patterns of CeO2 vs milling duration time

This project has received funding from the EURATOM research and training programme 2017-2021 under grant agreement No 755171. The content of this deliverable reflects only the author's view. The European Commission is not responsible for any use that may be made of the information it contains.

The various dissolution tests show that below 60 min of milling the effects on the dissolution are weak but remarkable since the dissolution rate rises from 0.1% to 6%. However, it is possible to observe the appearance of two regimes including for milling duration of 10 min allowing to achieve dissolution rates 60 times higher after only 10 min of milling. From a structural point of view, this improvement in kinetics may be related to the gradual increase of the full width at half maximum and therefore to the decrease in crystallite sizes with milling duration. The first regime of dissolution kinetics in red makes a high contribution to the total dissolution rate itself, it dissolves 25% out of the 41 in total. This contribution is reflected in particular on the recorded X-ray diffractogram, the full width at half maximum is greater but the shoulder to the left of the maxima is also more prominent. The shoulder identified as being linked to the nanoparticles increases significantly, which seems to indicate that the proportion of Ce^{3+} seems to contribute mainly to the first regime. Beyond 60 min of milling, no additional modification of the structure is brought in practice. The full width at half maximum of the CeO_{2-x} peaks of the 120 min ground sample is almost equivalent to that of the 60 min ground sample and the dissolution rates at 6 h between the 1 hour-milled sample and the 2h-milled one are similar.

The limits of the milling then dissolution process are reached for one hour of milling, beyond which the structural modifications are no longer sufficient to have an additional effect on the dissolution kinetics. The dissolution in concentrated nitric acid at 95 ° C of CeO2 calcined at 1200 ° C and ground cannot exceed 41% after 6 hours without milling again. Coupling will overcome this limitation by perpetually renewing the activation of the solid.

THE MILLER STIRRING SPEED

This speed corresponds to the rotational speed of the stirring shaft making moving the beads in the milling chamber. This parameter acts simultaneously on the number of contacts between the balls and on the intensity of collisions.

Three rotational speeds were chosen, 4200 rpm, which represents the maximum speed attainable by the equipment, 1000 rpm, which is the minimum speed to make the balls moving in the grinding chamber and an intermediate speed of 2500 rpm. The concentration and the speed of rotation of the peristaltic pump are fixed respectively at 4.67 $g.L^{-1}$ and 175 rpm.

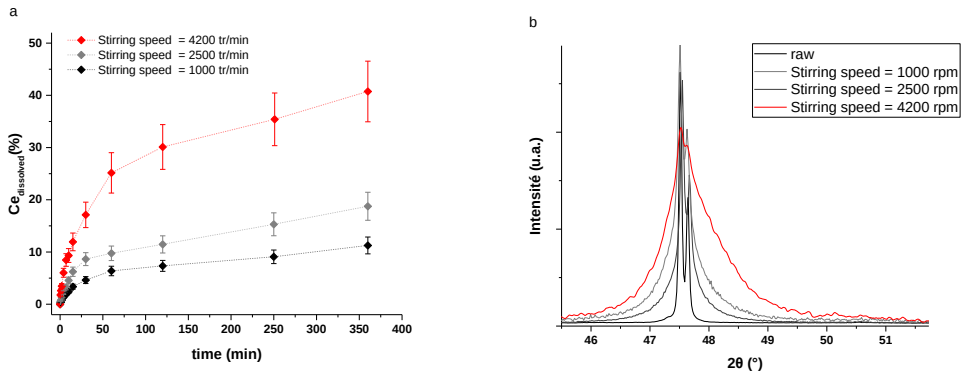

Figure 15 : ***a) kinetics rates of dissolution in [HNO_3] = 8.5 M et T=95°C of raw and milled ceria ([Ce]=4.67 $g.L^{-1}$, $t_{milling}$=60 min V_{pump}=175rpm) for different stirring speed. b) changes in X-ray diffraction patterns of CeO_2 vs stirring speed.***

This project has received funding from the EURATOM research and training programme 2017-2021 under grant agreement No 755171. The content of this deliverable reflects only the author's view. The European Commission is not responsible for any use that may be made of the information it contains.

After one hour of milling at these different shaft rotation speeds, the dissolution kinetics shown in **Figure 15** indicate final dissolution rates ranging from 11% for the lowest miller stirring speed to 41% for the maximum speed. This difference between the dissolution curves of stirring rates is also found on the profiles of the associated powder X-ray diffractograms. The full width at half maximum of the diffraction peaks of CeO_2 ground at 4200 rpm is much greater than those obtained from the diffractograms recorded from the other oxides ground at the other two miller stirring speeds. In addition, the asymmetry of the peak linked to the presence of nanoparticles are clearly greater to those of the other two agitation speeds as well as the dissolution rates.

This test demonstrates that efficient grinding is grinding with a high rotational speed, which will allow, by different breaking modes, the reduction of the size of the particles but also the generation of several types of defects.

THE SUSPENSION FLOW RATE

As the grinding operation is carried out continuously, the suspension circulates in a loop from the outlet of the chamber to the feed tank of the grinder. The flow rate of the suspension is one of the parameters that the operator controls via a peristaltic pump and which influences the residence time of the particles in the grinding chamber on each pass. This residence time (**Eq. 3**) per revolution is equal to:

$$\tau = \frac{V_{chamber} - V_{beads}}{fr_{susp}} \qquad \textbf{Eq. 3}$$

$V_{chamber}$: volume of empty grinding chamber;

V_{beads}: volume of the beads inside the grinding chamber;

fr_{susp} : suspension flow rate.

The suspension volume and the total time are initially set by the operator, an increase in the suspension flow rate leads according to **Eq. 3** to a decrease in the residence time of the suspension per pass, but on the contrary an increase in the number of renewals during the total time of the operation. Figure 16 makes it possible to convert the speed of rotation of the peristaltic pump, a parameter to be entered in the equipment, into suspension flow rate in $mL.min^{-1}$ and into residence time per revolution expressed in $s.rd^{-1}$.

This project has received funding from the EURATOM research and training programme 2017-2021 under grant agreement No 755171. The content of this deliverable reflects only the author's view. The European Commission is not responsible for any use that may be made of the information it contains.

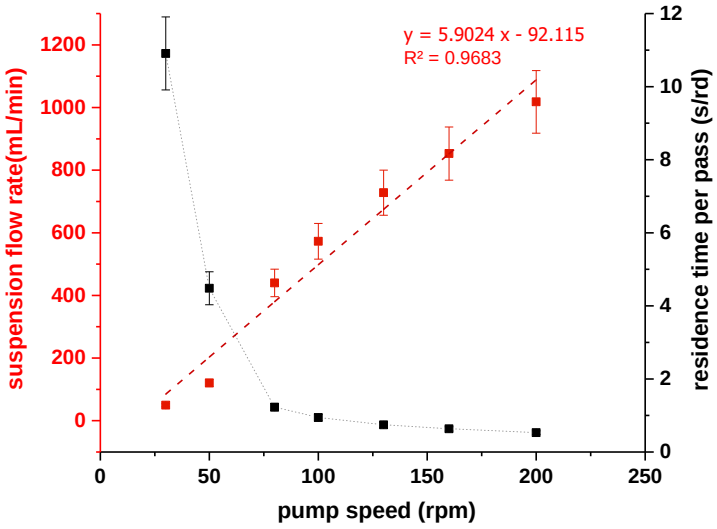

Figure 16 : relationship between the speed of peristaltic pump (rpm) and the suspension flow rate (mL.min^{-1}) or the residence time (s.rd^{-1}).

The flow rate influences the transport properties of the slurry such as the viscosity and homogeneity of the slurry and therefore influences the hydrodynamic conditions inside the grinding chamber. For a sufficiently low flow rate, problems with sedimentation of particles in the pipes or an accumulation of the product in the grinding chamber may appear which causes a rise in pressure and a stop of the operation.

The grinding tests carried out at different flow rates were intended to verify experimentally whether the flow rate has an influence on the solid and indirectly on the dissolution operation. Three separate flow rates corresponding to peristaltic pump rotation speeds ranging from 50 rpm to 175 rpm were tested with a maximum shaft rotation speed equal to 4200 rpm, a suspension concentration of 4.67 gL^{-1} and a duration of 60 min. Following these grinding tests, the dissolution kinetics on the samples of these grinding tests were measured and shown in Figure 17.

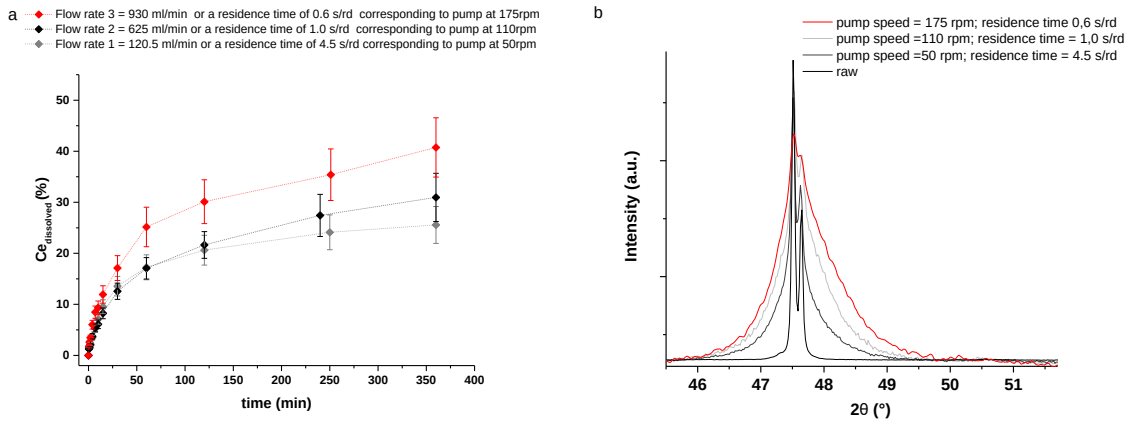

Figure 17: a) dissolution kinetics rate of CeO_2 after milling for 1 hour with a suspension concentration of 4.67 g.L^{-1} and a shaft rotation speed of 4200 rpm and different peristaltic pump rotation speeds ([HNO_3] = 8,5 M et T = 95°C) b) changes in XRD peaks depending on pump rotation speed or residence time per pass.

This project has received funding from the EURATOM research and training programme 2017-2021 under grant agreement No 755171. The content of this deliverable reflects only the author's view. The European Commission is not responsible for any use that may be made of the information it contains.

These kinetics demonstrate that the flow rate has little influence on the final dissolution rate. This lattest varies from 26 ± 4.7% to 41 ± 6.3%. The dissolution kinetics of the lowest flow rates are almost similar taking into account their uncertainty, but the kinetics with the highest flow rate stand out by being superior. The higher flow rate makes it possible to avoid the segregation of particles which would have sedimented in the circulation circuit and which would have been less well milled. These observations confirm that in the case of CeO_2 milling, the number of revolutions of the suspension in the grinder is the preferred factor and not the residence time.

These observations on the weak influence of the circulation flow rate on the grinding result agree or corroborate the observations of Gers et al. **[43]** made on the milling of calcite. The effect generated by the flow rate is very insignificant compared to the stresses resulting from the rotation of the stirrer shaft.

THE SUSPENSION CONCENTRATION

The concentration of the solid suspension is an important operating parameter for the sustainability of the process. Indeed, depending on the value of this parameter, the clogging of the filter present at the outlet of the grinding chamber will be more or less limited.

Figure 18 shows that the more the concentration of the suspension increases, the more the final dissolution rate decreases significantly. Indeed for a concentration of 4.67 gL^{-1} this rate reaches 41% but when this concentration is multiplied by 7 (33.3 gL^{-1}) the final dissolution rate reaches 12%, ie divided by 4. The diffractograms presented in *Figure 18*b) demonstrate that the FWHM of the diffraction peaks is smaller in the case of the most concentrated suspension. The more the concentration of the suspension increases, the less the solid is subjected to the effects of milling.

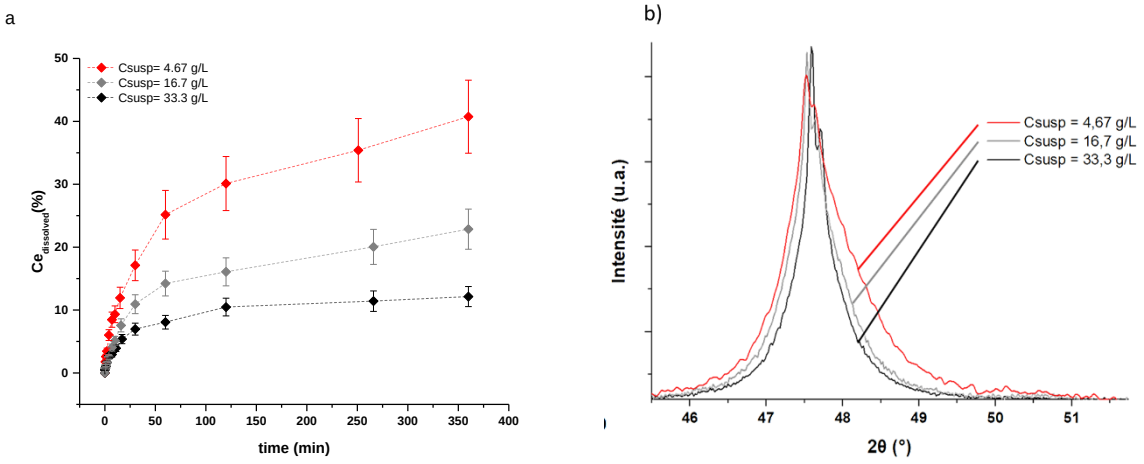

Figure 18 : a) kinetics rates of dissolution, in [HNO_3] = 8,5 M et T = 95°C, of milled ceria (stirring speed =4200 rpm ; t=60 min ; pump rotation speed =175 rpm) for different suspension concentrations b) changes in XR diffraction patterns vd suspension concentration.

This project has received funding from the EURATOM research and training programme 2017-2021 under grant agreement No 755171. The content of this deliverable reflects only the author's view. The European Commission is not responsible for any use that may be made of the information it contains.

Ouattara [44] demonstrated a greater fineness of the solid is obtained for low concentration. This result confirms the influence of the concentration in agreement with the results obtained by Varinot et al. [45], Bel fadhel et al. [46] and Garcia et al. [47]. In theory, the solid concentration influences the number of stresses (SN) undergone by a particle according to Eq. 4 :

$$SN \propto \frac{\varphi_{beads}\,(1-\varepsilon)}{[1-\varphi_{beads}(1-\varepsilon)]C_p} \cdot \frac{nt}{{d_{beads}}^2} \qquad \text{Eq. 4}$$

φ_{beads} : beads filling rate ;

ε : proportion of empty space within the chamber ;

n : rotation speed;

t : milling duration ;

d_{beads} : bead diameter;

Cp : suspension concentration.

The number of stresses is inversely proportional to the number of initial particles. As the particle concentration increases, the number of stresses on a particle decreases, so it is not surprising to observe an unfavorable effect of concentration on the milling result for a given specific energy.

These dissolution kinetics demonstrate that it is unnecessary to process too large amounts of solid at a time. When the suspension concentration is too high, the number of effective hits decreases. This part of powder neglected during milling, which increases with the concentration of the suspension, therefore not being activated, explains the decrease in dissolution rates. It will then be preferable during the coupling to add at regular intervals quantities of powder to be dissolved to renew the powder to be dissolved.

THE MILLING ENERGY

The activation energy of the solid is a parameter that results from the contribution of all the operating parameters mentioned above. This “supra-parameter” was set at 0.13 kWh (final energy) as part of this test. The other parameters listed in Table 5 such as the duration of the test, the speed of rotation of the stirring shaft or the flow rate were set so as to achieve the fixed grinding energy.

Table 5: different settings for a same final energy of milling.

This project has received funding from the EURATOM research and training programme 2017-2021 under grant agreement No 755171. The content of this deliverable reflects only the author’s view. The European Commission is not responsible for any use that may be made of the information it contains.

	Milling duration time (min)	Shaft stirring speed (rpm) (tr/min)	Milling power (kW) (kW)	Suspension flow rate (speed of pump)	Milling energy (kWh)	SSA (m^2/g)
R_1P_1	58	3761	0.14	55	0.13	37
R_2P_2	35	4200	0.25	170	0.13	28
R_3P_3	110	3500	0.05	130	0.13	19

The modification of the main milling parameters resulting in the same final milling energy of 0.13 kWh resulted in the production of three different materials. Analysis of the specific surface area highlights these differences, varying from 37 $m^2.g^{-1}$ to 19 $m^2.g^{-1}$ for the same milling energy.

When the milling duration time is long but the stirring speed is low (R3P3), the milling power is low and the specific surface area obtained is the lowest. The speed of rotation then seems to be the main parameter to control the power. However, the sample having intermediate milling conditions exhibits a higher specific surface area than the sample ground at high stirring speed but shorter milling time. A lesser but not negligible contribution of the milling time on the reduction of the size of the particles should therefore be noted. Structurally, the peaks of the X-ray diffraction patterns obtained for the samples from each of the milling tests have almost equivalent FWHM (Figure 19b).

The prolonged milling of CeO_2 leads to wear of the balls. In the present case, these balls are composed of zirconium oxide stabilized with yttrium, the diffraction peak of which is annotated with an * on the diagram R3P3 in Figure 19b.

Each of these three materials was dissolved under the same 8.5M HNO_3 conditions. The dissolution of these three materials is shown in Figure 19a.

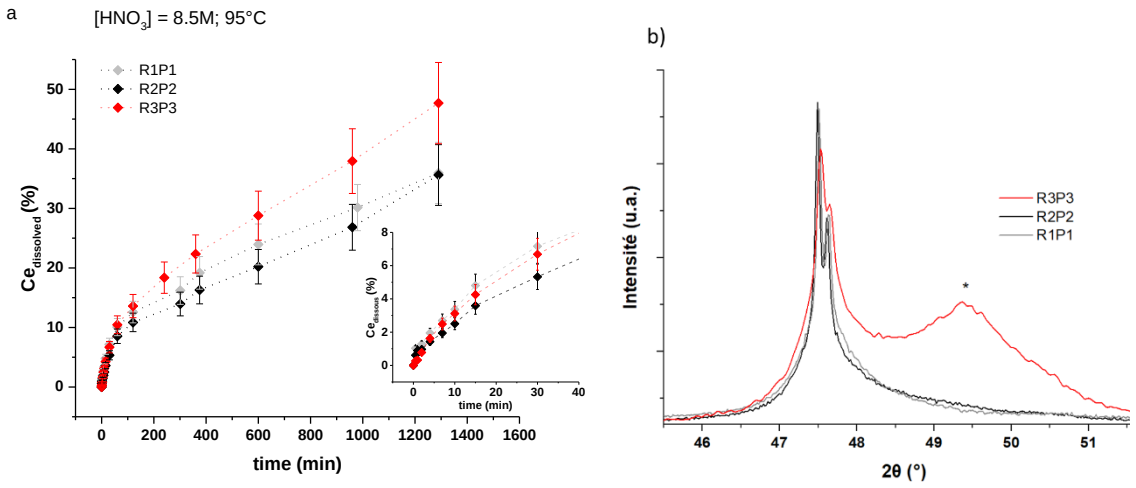

Figure 19: kinetics rates of dissolution of milled CeO_2 for different miller settings reported in Table 5. b) changes in X ray diffraction patterns of milled ceria depending on miller settings.

This project has received funding from the EURATOM research and training programme 2017-2021 under grant agreement No 755171. The content of this deliverable reflects only the author's view. The European Commission is not responsible for any use that may be made of the information it contains.

The modification of the main milling parameters resulting in the same final milling energy of 0.13 kWh resulted in the production of three different materials. When dissolution is studied during the first regime, ie during the first 30 minutes, the sample with the largest specific surface dissolves the fastest. At 30 min, R1P1 dissolves at 6% and has a specific surface area of 37 $m^2.g$-1. In the long term, this reasoning is no longer valid, it is the R3P3 sample, with a specific surface area of 19 $m^2.g$-1, which has better final dissolution rates.

For the same grinding energy of 0.13 kWh, the dissolution rates as well as the kinetics are different. For the coupling mode, setting would have to favor the first dissolution regime, milling should then be carried out with a fast milling shaft stirring speed.

CONCLUSION ON SOLID ACTIVATION BY HIGH ENERGY MILLING AND ITS EFFECT ON DISSOLUTION KINETICS

The use of the Micro Series grinder made it possible, through different stress modes applied to the sample, to provide sufficient grinding intensity not only to disagglomerate the reference CeO_2 particles but also to grind them. At first glance, this reduction in particle size results in an increase in the specific surface area from 0.7 to 29.5 $m^2.g^{-1}$. The combination of particle size data and microscopic observations led to the conclusion of a two-stage grinding mechanism. From the first moments, the impacts of the balls weaken the grain boundaries present in the platelets. As the grinding proceeds, as the size decreases, the grinding mechanism becomes transgranular.

A first population consists of grains of the order of a micrometer and with defects. These defects are linear and correspond to dislocations, which had not yet been reported in the literature for CeO_2 until now. They can both pass through crystallites, which will facilitate their rupture and decrease the size of coherent domains or accumulate near an impact point causing an increase in internal energy in the crystallite. The second population corresponds to nanoparticles. Their analysis by transmission electron microscopy and EELS indicates a core-shell effect as a function of size, with cerium on the surface at oxidation degree + III. It appears that for sizes less than 5 nm the particles are exclusively composed of Ce^{+3}.

Tests on the reference sample after grinding demonstrate a significant increase in dissolution kinetics. This increase in dissolution kinetics by a factor of 360 is partly explained by a decrease in the specific surface. However, not everything can be explained by this factor, another element provided by the grinding increases the kinetics of dissolution. Ziouane's model analysis made it possible by analogy to identify that the second regime is governed by the dissolution of particles containing dislocations reducing the size of coherent domains. The mechanism behind the first kinetic dissolution regime seems to be linked to the dissolution of partially reduced nanoparticles. However, this could not be clearly established.

The modification of certain grinding parameters made it possible to maximize the first dissolution rate. The grinding time has notably made it possible to realize that beyond 60 min the additional effects generated by the grinding on the solid are negligible, resulting in dissolution rates that do not exceed 41% after 6 h. The limits of the grinding then dissolution process having been reached, the coupling process therefore appears as the solution to keep the activation of the solid until it is completely dissolved.

MILLING-DISSOLUTION COUPLING PROCESS

This project has received funding from the EURATOM research and training programme 2017-2021 under grant agreement No 755171. The content of this deliverable reflects only the author's view. The European Commission is not responsible for any use that may be made of the information it contains.

In the previous chapter, the study of dissolution kinetics and diffractograms demonstrated the limit of the milling time, marking the limit of the decoupled process of grinding then dissolution. From the grinding point of view, beyond 60 min of grinding under the defined conditions, the solid is no longer sensitive to the effects of grinding and this results in dissolution kinetics equivalent to that obtained on the ground material for 60 min. From the point of view of the dissolution It seems that the grinding also has a very important impact during the first hour of dissolution, then its effect decreases but the kinetics of dissolution beyond one hour remain however higher than that of a material not previously activated. In other words, during dissolution, the activated material will gradually passivate, reducing the dissolution kinetics without returning to its initial state before grinding. Indeed, the presence of residual dislocations distinguishes this material from the unground solid. However, the dissolution kinetics obtained on this decoupled process remain insufficient to allow total dissolution within a reasonable industrial time. This is why it is necessary to study the grinding / dissolution coupling in order to continuously renew during dissolution the activation of the surface of the material to be dissolved.

Thus in this part, several coupling tests were carried out in order to improve the dissolution rate of the reference oxide. A first test was carried out under conditions comparable to those carried out in the dissolution reactor but in a slightly corrosive chemical attack medium ([HNO_3] = 0.5 M and T = 50 ° C). Subsequently, the quantities of material were reduced to be representative of the conditions implemented during the tests of the decoupled process of grinding then dissolution.

The behavior of the material on dissolution during coupling will then be compared to that previously described during the decoupled process in order to deduce a reaction mechanism.

Finally, the last part presents tests aimed at improving the grinding / dissolution coupling process in an attempt to achieve total dissolution of the solid. The grinding parameters having already been optimized in the previous chapter, only the influence of acidity was tested.

MILLING-DISSOLUTION COUPLING PROTOCOL

The tests in the milling and dissolution coupling configuration were carried out in the grinder. Just like the milling tests, the chamber is filled to 85% by volume with beads of a size of 0.6 mm then closed using a support allowing the suspension to circulate through a sieve of. 0.2 mm.

When the assembly is complete, 300 mL of nitric acid were introduced into the mill circuit via the sampling tank. The peristaltic pump as well as the agitation of the balls were started in order to reach the set value. The oxide was then introduced through the sampling tank. It is at this given moment that the chronometer was started for the follow-up of the sampling during the coupling test.

Each suspension sample was placed in a 0.6 mL cone and immersed for a few seconds in an ice-cold water bath in order to stop the kinetics of the dissolution reactions (thermally activated reaction). To analyze only the solution and to avoid analyzing measurement biases linked to the presence of colloids, the suspension was centrifuged for 10 min and then left to stand for 10 min to allow sedimentation of the particles set in motion. Only 0.4 mL were pipetted on the surface to be diluted in a flask and analyzed by ICP-AES.

In the previous chapter, several parameters were tested in order to find the optimum grinding configuration for cerium oxide. Apart from the size of the beads and the rate of loading of the chamber with beads, only three parameters can be modified by the experimenter. The flow rate of the suspension and the stirring speed are set directly on the control panel of the mill, while the initial concentration of the suspension is set

This project has received funding from the EURATOM research and training programme 2017-2021 under grant agreement No 755171. The content of this deliverable reflects only the author's view. The European Commission is not responsible for any use that may be made of the information it contains.

according to the experiment. For these grinding / dissolution coupling tests, the beads were rotated at a speed of 4200 rpm and the suspension circulated so that the suspension remained in the chamber for 0.6 sec at each revolution.

In this part, the coupling tests were carried out at a temperature close to 50 ° C. This choice is explained by the fact that this temperature is the temperature induced by friction during a milling test under these conditions. Just like the acoustic cavitation phenomena observed in sonochemistry **[48]**, when a ball comes into contact with the particle, an intense pressure is produced at the point of impact. Part of the energy associated with the shock is transmitted to the particle to fragment it or induce defects, and another is converted into heat. It is this same heat that is used in the mechanosynthesis of certain mechanical alloys, among others **[49]**.

MILLING-DISSOLUTION COUPLING TESTS

EFFECTS OF DISSOLUTION CONDITIONS

TEST AT 20g.L^{-1} OF CERIA

This concentration corresponds to that established during the dissolution tests carried out on the milling then dissolution process. During these tests, the concentration of the suspension was 20 gL^{-1} thus the milling and dissolution coupling test was adapted to respect this concentration, i.e. 6 g of reference CeO_2 were ground and simultaneously dissolved in 300 mL of acid. nitric at 0.5 M.

The ICP-AES analysis of each of the samples taken led to the dissolution kinetics presented in **Figure 20**. This kinetics curve is compared to that of ungrounded reference CeO_2 and ground for 1 h then dissolved under the same chemical attack conditions.

These first tests were carried out in a weakly concentrated acid ([HNO_3] = 0.5 M and T = 50 ° C) in order to avoid premature wear of the equipment and in particular of the grinding chamber. Under these conditions, no equipment alteration was observed following this first test.

This project has received funding from the EURATOM research and training programme 2017-2021 under grant agreement No 755171. The content of this deliverable reflects only the author's view. The European Commission is not responsible for any use that may be made of the information it contains.

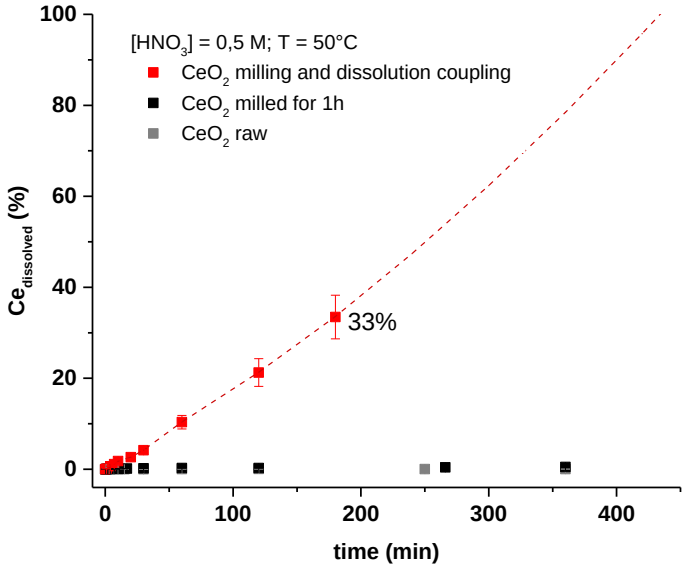

Figure 20 : comparison of the kinetic dissolution curves in the reactor configuration (20 gL-1) of (in gray) raw CeO_2, (in black) milled for 1 h reference CeO_2 and (in red) reference milled and dissolved simultaneously CeO_2 during the first milling / dissolution coupling test.

Under these same dissolution conditions, the reference cerium oxide (unground) remains completely refractory to dissolution reactions. The first dissolution tests which were presented in chapter III resulted in a dissolution rate after 6 h of 0.1% for more corrosive conditions ([HNO_3] = 8.5 M and T = 95 ° C). Under less corrosive conditions the amounts of dissolved solids are so low that they cannot be detected by ICP-AES.

Ground reference CeO_2 for 1 hour follows the kinetics of dissolution in 0.5 M HNO3 at 50 ° C shown in black on the **Figure 20**. Just like the dissolution kinetics of the ground reference oxide for 1 hour presented in Chapter III, it occurs in two regimes but only makes it possible to reach 0.5% of dissolved oxide after 6 hours of dissolution.

Coupling, for its part, demonstrates the interest of such a process (**Figure 20**). It makes it possible in a shorter time to achieve a dissolution rate much higher than that of the decoupled process. After 3 h, the dissolution rate reaches 33% against 0.5% after 6 h of dissolution after a grinding step of one hour in water.

Unlike the decoupled process whose dissolution kinetics are made up of two distinct regimes reflecting the progressive passivation of the activated solid, the coupling has only one regime which can be described according to a second degree polynomial with a regression coefficient R^2 of 0.9997:

$$\%Ce = 1,676 \times 10^{-4}\, t^2 + 1,576 \times 10^{-1}\, t \qquad \text{Eq. 5}$$

This project has received funding from the EURATOM research and training programme 2017-2021 under grant agreement No 755171. The content of this deliverable reflects only the author's view. The European Commission is not responsible for any use that may be made of the information it contains.

By extrapolation of this equation, it would take around 430 min or nearly 7 h to reach a dissolution rate of 100%. For a material ground for one hour and then dissolved under more drastic conditions (8.5 M and 95 ° C), the dissolution rate reached after 7 h is only 41%.

In the previous chapter aimed at improving grinding, it is the lower suspension concentrations that allow higher dissolution rates to be obtained. This test was carried out with suspension concentrations identical to those used in the grinding part of the decoupled process, ie 20 gL^{-1}. This is why the following part will detail a new coupling test with a suspension concentration of 4.6 gL^{-1}. Such a value will make it possible to be representative of the conditions used during the grinding tests and should make it possible to improve the dissolution kinetics of the coupling process.

TEST AT 4.6g.L^{-1} OF CERIA

During the milling tests presented in the decoupling process, the concentration of the powder suspension was 4.6 gL^{-1}. The milling / dissolution coupling test was adapted to respect this concentration. Thus, 1.4 g of reference CeO_2 were ground and simultaneously dissolved in 300 mL of 0.5 M HNO3. The aim of this experiment was to verify whether the dissolution rates achieved by the coupling process under these conditions are greater than those of the previous test as suggested by the decoupling study.

The analysis by ICP-AES of each of the samples taken led to the kinetics presented **Figure 21**. This kinetics is compared with that of ungrounded reference CeO_2 and ground for 1 h under the same conditions of chemical attack and suspension concentration.

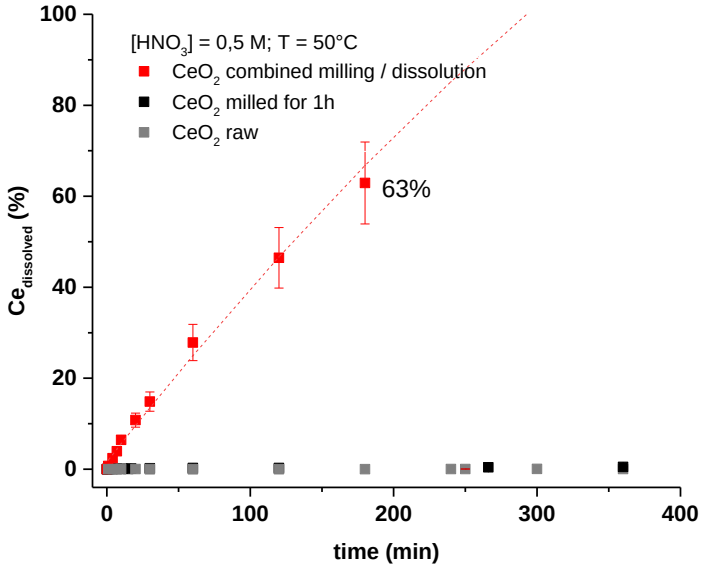

Figure 21 : comparison of the dissolution kinetics in the mill configuration (4.6 gL^{-1}) of (in gray) raw reference CeO_2, (in black) milled for 1h reference CeO_2 and (in red) simultaneously milled and dissolved reference CeO_2 for a suspension concentration of 4.6 gL^{-1}.

This project has received funding from the EURATOM research and training programme 2017-2021 under grant agreement No 755171. The content of this deliverable reflects only the author's view. The European Commission is not responsible for any use that may be made of the information it contains.

As the reference cerium oxide has not undergone any structural and microstructural modifications by grinding, it is consequently not dissolved just as in the previous part. This material remains refractory for any type of leaching solution. The dissolved cerium concentrations are below the detection limits of analytical equipment.

When ground 1 h (black kinetics **Figure 21**) and dissolved in this medium only 0.5% of the cerium oxide was solubilized. This value is identical to that of the dissolution test carried out in the previous part for a concentration of 20 gL^{-1}. For a low concentration of nitric acid and in the case of a decoupled process, the quantity of ground solid introduced into the dissolution reactor does not seem to have an influence on the kinetics.

After 3 h of coupling, it is possible to solubilize 63% of the cerium which initially was in the form of an insoluble refractory material under such conditions. It makes it possible in a shorter time to achieve a dissolution rate that is significantly higher than that of the decoupled process. The influence of the concentration of the initial suspension is also verified; this parameter should be minimized in order to increase the dissolution kinetics. Thus, in an industrial process, successive additions of oxide to be dissolved would have to be carried out rather than introducing large quantities of oxide initially for the same volume of acid.

PHENOMENUM ELUCIDATION

In the previous chapter, microscopic observations by scanning and transmission electron microscopy led to the conclusion that the activation of CeO_2 takes place according to two regimes. During the first moments, the solid fragments by decohesion of the solid at the level of the grain boundaries and causes the density of the latter to decrease. Gradually the size decreases with the increase in milling time and the rupture mechanism becomes mainly transgranular. The transition between these two regimes takes place between 30 and 40 min of milling and makes it possible after 1 h to achieve nanoparticles of around 10 nm. Grinding with a high stress intensity makes it possible to reduce the size of the particles down to the nanometric scale causing the appearance of Ce^{3+} and generating the creation of structural defects (dislocations). Each of these contributions allows the solid to be more easily dissolved (gray curve **Figure 22**).

This project has received funding from the EURATOM research and training programme 2017-2021 under grant agreement No 755171. The content of this deliverable reflects only the author's view. The European Commission is not responsible for any use that may be made of the information it contains.

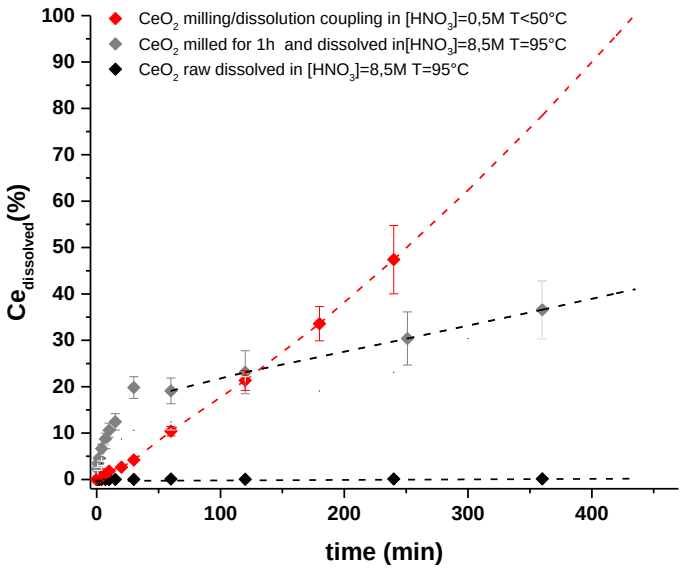

Figure 22 : dissolution kinetics of the milling / dissolution coupling test (0.5M;T = 50 ° C and suspension concentration of 20 gL^{-1}) and of the milling then dissolution test (8.5M and T = 95 ° C).

The kinetics of the reference oxide activated then dissolved at 95 ° C in concentrated nitric acid consists of two regimes, the first of which is faster. The effect of this first regime gradually diminishes to the point that there is a break in slope and a second regime which is markedly slower. No analysis technique makes it possible to identify precisely which of these two contributions is mainly responsible for this acceleration. However, the study carried out from the model made it possible by analogy to determine the majority contribution to the second regime by micron particles containing defects.

Unlike the decoupled process, the simultaneous milling and dissolution of CeO_2 is not limited to the dissolution of the activated part of the solid which no longer exhibits any additional structural modification beyond one hour. The particle size during a process coupling milling and dissolution continues to decrease while the full

This project has received funding from the EURATOM research and training programme 2017-2021 under grant agreement No 755171. The content of this deliverable reflects only the author's view. The European Commission is not responsible for any use that may be made of the information it contains.

width at half maximum of the X-ray diffraction peaks obtained on samples after different milling / dissolution

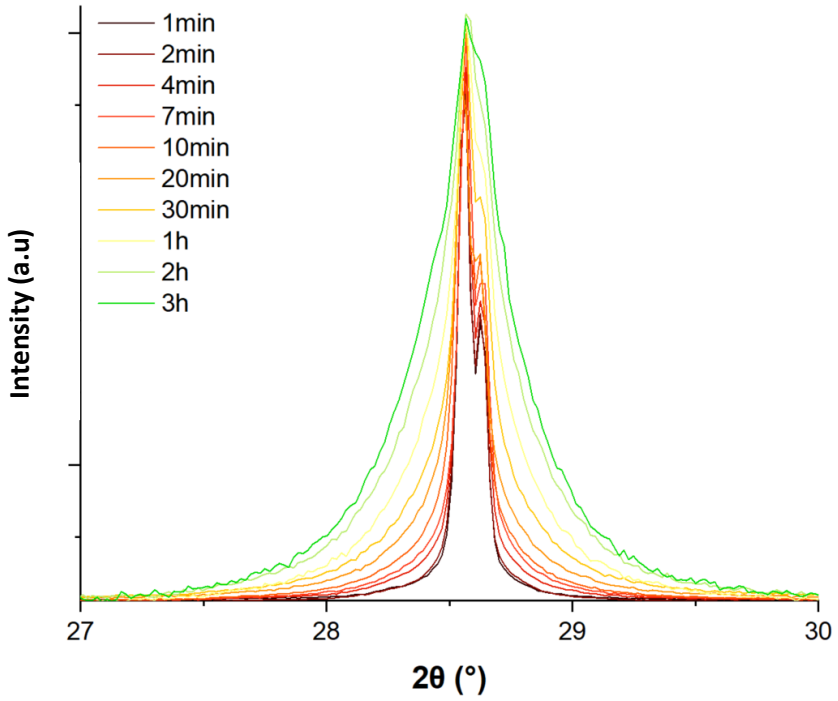

times increases as illustrated

Figure 23. This full width at half maximum continues to increase, even after 1 hour.

This project has received funding from the EURATOM research and training programme 2017-2021 under grant agreement No 755171. The content of this deliverable reflects only the author's view. The European Commission is not responsible for any use that may be made of the information it contains.

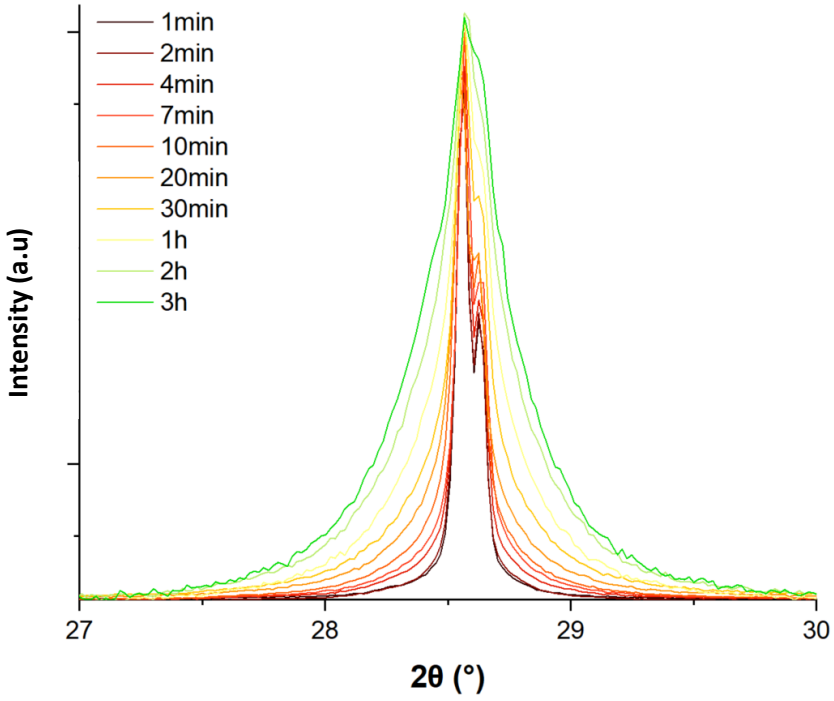

Figure 23: change in the full width at half maximum of a reference solid CeO_2 diffraction peak at different simultaneous milling / dissolution times (0.5M and T = 50 ° C and 20 gL^{-1}).

Coupling has the advantage of being able to modify the solid both by grinding (two-stage rupture mechanism) but also by dissolution (shrinking core model). Kinetics in red *Figure 22* which represents the coupling is slower before 1 h then accelerates. This latency period is linked to the initiation of the effects of the grinding of the reference oxide. It takes 40 min for the size reduction to be significant enough to start forming nanoparticles.

If this kinetics, which can be simulated by means of a polynomial of degrees 2, is reduced to two linear regimes, the equations of the associated slopes are referenced in the **Table 6**. The equation for the slope before 40 min is much lower than that beyond this time, meaning that the dissolution increases after 1 h.

Table 6: slope equations simulating the milling / dissolution coupling kinetics (0.5M and T = 50 ° C and 20 gL-1) if this is split into two regimes.

This project has received funding from the EURATOM research and training programme 2017-2021 under grant agreement No 755171. The content of this deliverable reflects only the author's view. The European Commission is not responsible for any use that may be made of the information it contains.

		Equation of the fit (%dissolved.min^{-1})	R^2
raw CeO_2	t < 40 min	$\%Ce_{dissolved} = 1.36\ 10^{-1}\ t + 1.01\ 10^{-1}$	0.987
Milling/dissolution coupling	t > 40 min	$\%Ce_{dissolved} = 2.05\ 10^{-1}\ t + 2.63\ 10^{-1}$	0.997

		Equation of the fit (%dissolved.min^{-1})	R^2
raw CeO_2	t < 40 min	$\%Ce_{dissolved} = 1.36\ 10^{-1}\ t + 1.01\ 10^{-1}$	0.987
Milling/dissolution coupling	t > 40 min	$\%Ce_{dissolved} = 2.05\ 10^{-1}\ t + 2.63\ 10^{-1}$	0,997

To better understand how the dissolution kinetics differ during the milling / dissolution coupling, the X ray diffractogram of the milled solid 1h is compared (24) to that of the residue taken at 1 hour during the coupling (in suspension condition of 4.6 gL^{-1}).

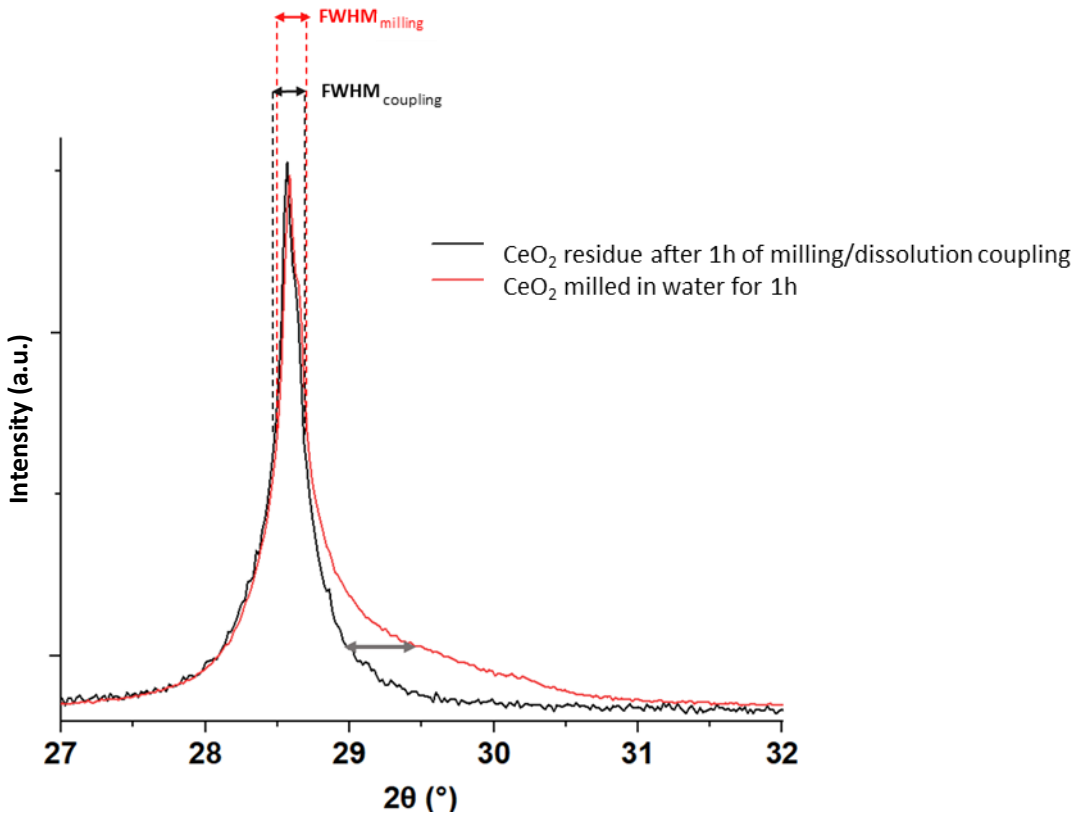

Figure 24 : superposition of the X-ray diffraction peaks of 1 hour ground CeO_2 (in red) and of the solid residue taken at 1 hour during the milling / dissolution coupling test (0.5M and T = 50 ° C and 20 gL^{-1}).

This project has received funding from the EURATOM research and training programme 2017-2021 under grant agreement No 755171. The content of this deliverable reflects only the author's view. The European Commission is not responsible for any use that may be made of the information it contains.

According to Scherrer's law, the full width at half maximum (FWHM) of a diffraction peak is inversely correlated with the size of the coherent domains. On the Figure 24 the diffraction peak of the ground solid (FWHM milling) is superimposed on that of the residue obtained after 1 hour of milling and simultaneous dissolution in nitric acid (FWHMcoupling) according to their relative intensity. This comparison highlights the structural difference between these two solids. The FWHMcoupling width obtained from the residue resulting from the milling / dissolution coupling is slightly greater than that of the ground sample (FWHMmilling). These two oxides having both been ground under the same conditions, they should exhibit equivalent FWHM. The difference can therefore only be linked to the effect of the dissolution, as a reminder one is milled in water then dissolved while the other has been milled and dissolved simultaneously in nitric acid at 0.5 M and at 50 ° C.

The gray arrow on the Figure 24 makes it possible to highlight the major difference between these two samples: the asymmetry to the right of the maxima Kα2. This asymmetry is not present in the case of the oxide ground in the acid.

This shoulder is described in the previous chapter as being related to nanoparticles of mixed CeO_2 / Ce_2O_3 composition and supported by experimental results from the literature **[37; 50]**. This asymmetry is not present in the case of the residue taken during the coupling grinding / dissolution of CeO_2. This difference can be interpreted as the absence of a nanoparticle. Their absence is linked to their consumption during the dissolution phenomenon.

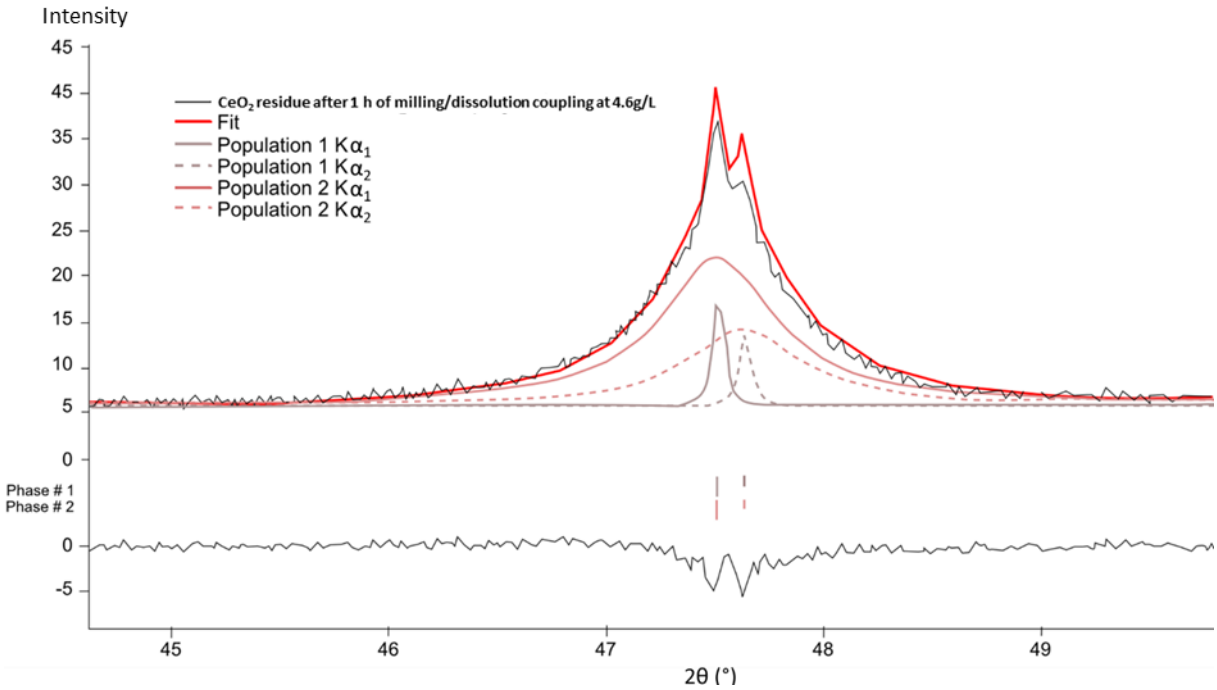

Figure 25 : decomposition of the X-ray diffraction peaks according to the presence of two populations at the end of the simultaneous grinding and dissolution of CeO2 under suspension conditions of 4.6 gL-1 in [HNO3] = 0.5 M and T = 50 ° C.

This project has received funding from the EURATOM research and training programme 2017-2021 under grant agreement No 755171. The content of this deliverable reflects only the author's view. The European Commission is not responsible for any use that may be made of the information it contains.

By refining the X-ray diffractogram on powder obtained from the oxide dissolved by grinding / dissolution coupling (*Figure 25*), two populations were highlighted. The sizes of the coherent domains being particularly high (of the order of a hundred nanometers), at the limit of the maximum resolution of a diffractometer, no size will be announced for the sake of accuracy and in order not to establish a biased interpretation. However, the breakdown of the contributions makes it possible to estimate two populations, one at the micron scale and the other at the nanometer scale.

The agreement of the positions in 2θ of these two populations indicates that they both have the same lattice parameter, namely that of cubic CeO_2: 5.4101Å.

According to Zhang et al.**[36]** nanoparticles whose size is greater than 40 nm do not incorporate Ce^{3+}, their lattice parameter therefore does not increase as described in the literature. By analogy, the second population has a size greater than 40 nm but no value can be precisely determined by refinement.

The absence of Ce^{3+} and of particles smaller than 40 nm which are nevertheless present during grinding in water as could be analyzed by DLS (average size of 10 nm) can only be explained by their dissolution by the acid.

All of these observations lead to the identification of a mechanism, during the grinding / dissolution coupling, mainly governed by the dissolution of the reduced nanoparticles.

The solid suspended in an acidic medium reaches the grinding chamber and is gradually fragmented. The grains are torn off by decohesion just as happens during grinding in water. Together these grains are dissolved according to the model of the shrinking heart. Although this model describes the progressive reduction of the surface linked to corrosion, the reference oxide is calcined at 1200 ° C therefore highly refractory (cerium concentration not detected after 6 h in $[HNO_3]$ = 8.5 M and T = 95 ° C), its dissolution therefore remains limited.

Beyond 40 min, the phenomena of breaking of the smallest particles and abrasion of the largest generate nanoparticles. Their size reaches for the smallest 10 nm when the grinding occurs in water.

However, the sample taken during the experiments coupling grinding and dissolution in acid and analyzed by DRX shows that there is no shoulder to the left of each diffraction peak and therefore nanoparticles of this size order at 1. h. However, the slope corresponding to the dissolution of CeO_2 increases well for these periods.

Thus these results converge towards the same conclusion, during the coupling as well as during a simple grinding, the size of the particles will gradually decrease. In the case of the grinding / dissolution coupling, this reduction is also caused by the dissolution. This dissolution is accelerated after 40 min by the formation and simultaneous dissolution of the smallest nanoparticles (less than 40nm).

This process has the advantage over simple grinding of having a particle size, for an instant t, smaller, which promotes the dissolution of such a refractory material but does not lead to complete dissolution after 3 h in the case of an acidity of 0.5 M. This is why the following part will detail the optimization of the milling / dissolution coupling conditions.

OPTIMIZATION OF MILLING-DISSOLUTION COUPLING PROCESS VIA CHANGES IN ACID CONCENTRATION

This project has received funding from the EURATOM research and training programme 2017-2021 under grant agreement No 755171. The content of this deliverable reflects only the author's view. The European Commission is not responsible for any use that may be made of the information it contains.

The grinding capacities were optimized in chapter III thus leading to coupling tests the aim of which was to achieve total dissolution in less than 3h. The tests presented in the previous part show that this rate is not reached for so-called mild attack conditions, that is to say for a nitric acid concentration of 0.5 M and a temperature of 50 °C.

First, we wondered about the minimum quantity of protons necessary for the dissolution of the oxide in order to compare it with what was introduced in these first coupling tests under so-called soft conditions. Indeed, an acid defect could also explain a partial dissolution. For a suspension concentration of 4.6 gL^{-1}, the number of mol of cerium is 8.1. 10^{-3} mol and for a concentration of 20 gL^{-1} it is 3.5. 10^{-2} mol. The coupling tests are carried out in [HNO3] = 0.5 M, ie a number of moles of H + of 0.15 mol. **Eq. 6** describes the dissolution of CeO_2.

$$CeO_2 + 4\,H^+ \rightarrow Ce^{4+} + 2\,H_2O \qquad \text{Eq. 6}$$

Thus for a suspension concentration of 20gL^{-1}, 0.14 mol of protons would be consumed to allow total dissolution against 0.15 available, and for a concentration of 4.6 gL^{-1} it would take 0.032 mol. If the quantity of protons present is strictly sufficient, the consumption of protons has a very large impact on the acidity of the medium, which explains why the dissolution is not complete under these chemical conditions. Certainly, if we consider that the major part of the dissolved Ce is at valence + III and not + IV, the consumption of protons is less but remains very impacting for the attack medium, the quantity of H + necessary for the dissolution would be three times the number of moles of Ce^{3+}, according to **Eq. 7**:

$$\boldsymbol{CeO_2 + 3\,H^+ + {}^1\!/_2\,H_2O \rightarrow Ce^{3+} + 2\,H_2O} \qquad \text{Eq. 7}$$

Thus the medium would go from 0.5 M to 0.15 M in the case of a suspension at 20 gL^{-1} after complete dissolution. For such a process, it cannot therefore be considered that the medium changes during the milling / dissolution coupling.

To overcome this problem, the chemical attack medium has been progressively hardened so as to find a compromise between an effective process and an attack medium limiting the corrosion of the equipment. This part therefore describes coupling tests with different acidities in order to achieve complete dissolution of CeO_2 in less than 3 h.

For this, two other tests were carried out with an initial suspension concentration of 4.6 gL^{-1}. The acidities chosen are 8.5 M corresponding to the acidity used during the grinding then dissolution tests and an intermediate acidity of 4 M.

This project has received funding from the EURATOM research and training programme 2017-2021 under grant agreement No 755171. The content of this deliverable reflects only the author's view. The European Commission is not responsible for any use that may be made of the information it contains.

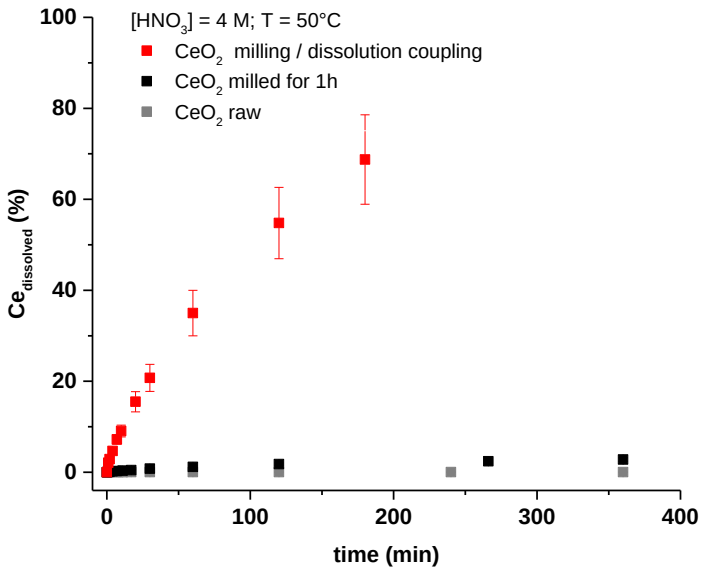

Figure 26: comparison of the dissolution kinetics at 4 M in nitric acid and 50 ° C for the raw reference oxide (in gray), the oxide milled for 1 hour (in black) and in the milling / dissolution coupling configuration (in red).

Dissolving the unground reference oxide in 4 M nitric acid (in gray on the **Figure 26**) is not detected by the ICP due to the dissolved infinitesimal quantities. Grinding and its effects have little impact on the dissolution rate, which reaches 3% after 6 hours. For such low dissolved cerium concentrations it seems and in view of the uncertainties that it is not possible to state that this kinetics is in two regimes like that described in the previous chapter.

Coupling, for its part, has a much higher dissolution rate than the decoupled process (in gray on the **Figure 26**). It makes it possible to achieve in 3 h a higher dissolution rate than that of the process coupled with lower acidity, ie 67%. As total dissolution was not achieved at 4 M, the acidity was increased to 8.5 M.

Under these conditions (8.5 M and T = 50 ° C) the reference material has still not been dissolved. Activation of the solid by grinding for one hour made it possible to increase the dissolution rate to 5% at 50 ° C. Finally, the coupling test is conclusive, it makes it possible to achieve a dissolution rate of 86% after 3 hours. This value is markedly higher than that of the decoupled process operating at 95 ° C., which only makes it possible to reach 38% dissolved in 6 h. Taking into account the uncertainties (12% relative) this dissolution under conditions of coupling grinding / dissolution in 8.5 M HNO_3 medium at 50 ° C is almost total (Figure 27).

This project has received funding from the EURATOM research and training programme 2017-2021 under grant agreement No 755171. The content of this deliverable reflects only the author's view. The European Commission is not responsible for any use that may be made of the information it contains.

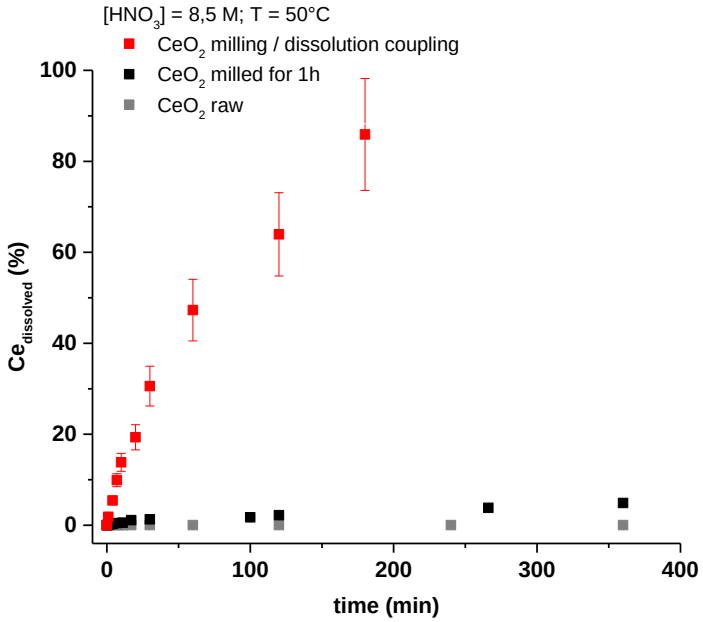

Figure 27 : comparison of the dissolution kinetics at 8.5 M in nitric acid and 50 ° C for the raw oxide (in gray), the oxide milled for 1 hour (in black) and in dissolution coupling configuration (in red).

Comparison of the dissolution kinetics of the various grinding / dissolution coupling tests illustrated Figure 28 highlights the effect of acidity on the process.

This project has received funding from the EURATOM research and training programme 2017-2021 under grant agreement No 755171. The content of this deliverable reflects only the author's view. The European Commission is not responsible for any use that may be made of the information it contains.

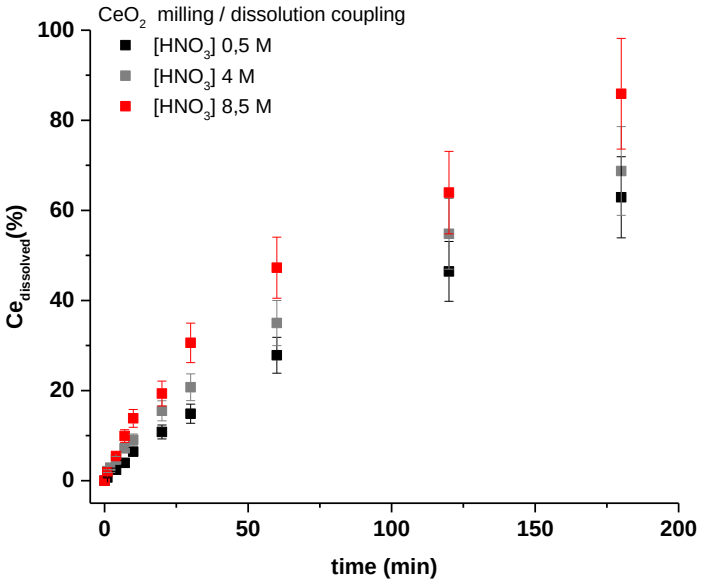

Figure 28 : comparison of the kinetics during the various milliing / dissolution coupling tests for different acidities (0.5M: black, 4M: gray and 8.5M: red) with a concentration of 4.6 gL-1, a stirring speed balls of 4200 rpm-1, a flow rate of 170 rpm-1 and a temperature of 50° C

As shown in the **Figure 28**, before 30 min of grinding / dissolution, the dissolution rates are hardly different and whatever the acidity, they do not exceed 20%. Structurally this results in a similar width at mid-height of the diffraction peaks for each sample of each test. At the start of the coupling, a certain latency time is necessary to modify the properties of the solid. On the **Figure 29a** the different FWHM are equal to that obtained from the unground solid, it is necessary to wait 7 min to begin to notice the effects of the milling (**Figure 29b**). However, differences appear between the reference oxide (t = 0 min) and the milled / dissolved oxides. However, since there is no difference between the FWHMs for each acidity, this means that only milling has changed the structure and the acidity-related effects are not yet felt.

It is not until 30 minutes that the structural changes depend on the acidity. On the **Figure 29c** the largest FWHM corresponds to the highest acidity and gradually decreases for 4 and 0.5 M. These structural differences are also reflected in terms of kinetics where the difference between the dissolution rates widens. This observation continues until 3 h when the dissolution rates reach 86%, 69% and 62% corresponding to the acidity of 8.5 M, 4 M and 0.5 M respectively. Just like at 30 min the widths halfway up the **Figure 29d** reflect the progressive shrinkage of the coherent domains and therefore of the particles with time and acidity.

This project has received funding from the EURATOM research and training programme 2017-2021 under grant agreement No 755171. The content of this deliverable reflects only the author's view. The European Commission is not responsible for any use that may be made of the information it contains.

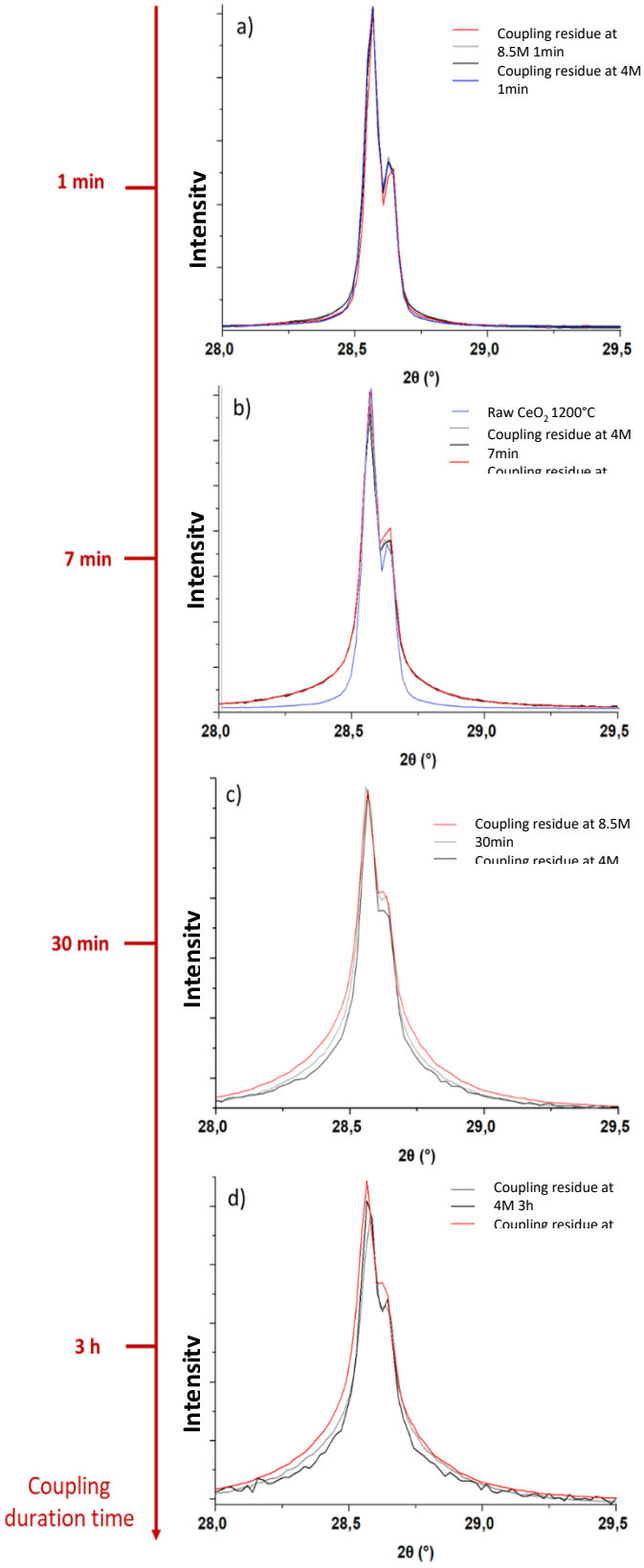

Figure 29 : evolution of the X-ray diffraction peaks of samples taken during milling / dissolution couplings at different acidities.

This project has received funding from the EURATOM research and training programme 2017-2021 under grant agreement No 755171. The content of this deliverable reflects only the author's view. The European Commission is not responsible for any use that may be made of the information it contains.

In the previous chapters the grinding has been optimized by independently studying the influence of each parameter. Thus the grinding time, the flow rate and the concentration of the suspension and the stirring speed have reached their limit. The dissolution aspect of the grinding / dissolution process was then optimized to achieve almost total dissolution of CeO_2. The coupling test achieves a dissolution rate of up to 86% (± 12%) at 3 h when the acidity is increased to 8.5 M. However, it may still be necessary to improve the process by varying the temperature of the solution or adding new acid to maintain the acidity despite its consumption during the quantitative dissolution of the material.

The **Figure 30** compares the dissolution kinetics of ground reference CeO_2 1 h (red) at 95 ° C and (black) at 50 ° C. The kinetics, although exhibiting both, two regimes are different with respect to the rate of dissolution. After 6 h of dissolution, the final dissolution rate is 37% at 95 ° C against 5% at 50 ° C. Thus the acidity is a less preponderant factor than the temperature for the improvement of the grinding / dissolution process as observed by other authors.[168]. Subsequently, to optimize the coupling process, higher temperature tests should be favored. This would require modifications to the grinding device by replacing the sampling tank with a thermostated tank with a double jacket connected to a thermostated bath. This explains why these tests were not privileged during this work in favor of a study on acidity.

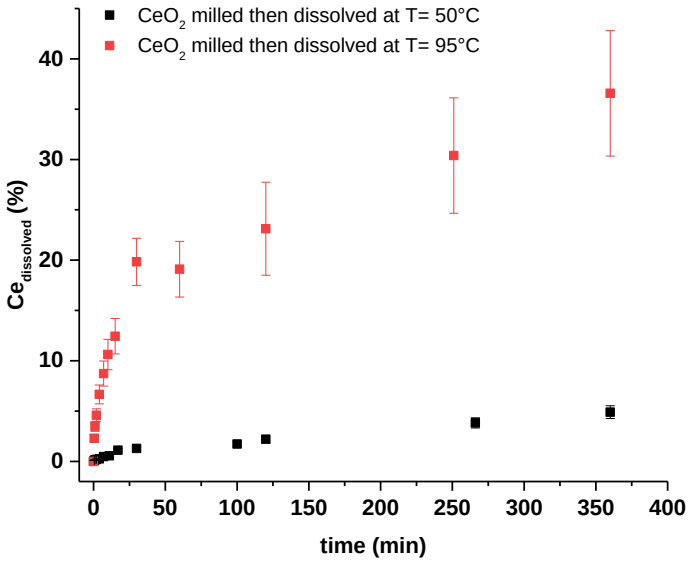

Figure 30: kinetics of dissolution of the ground reference oxide 1 hour dissolved in HNO_3 = 8.5 M at (in black) 50 ° C and (in red) at 95 ° C.

However, a compromise must be found between a 100% dissolution rate in the shortest possible time and attack conditions which will not damage the equipment.

CONCLUSION ON MILLING-DISSOLUTION COUPLING PROCESS DEVELOPMENT

In this chapter a first study on the grinding dissolution coupling was carried out for CeO_2. Initial tests carried out with a concentrated solution (20 gL^{-1} in 300 mL of HNO_3) under mild chemical attack conditions ([HNO_3] = 0.5 M and T = 50 ° C) led after 3 h to a dissolution rate of 33% much higher than the 0.5% achieved with simple

This project has received funding from the EURATOM research and training programme 2017-2021 under grant agreement No 755171. The content of this deliverable reflects only the author's view. The European Commission is not responsible for any use that may be made of the information it contains.

grinding (at 6 h). To increase the rate of dissolution, the concentration of the suspension was reduced to 4.6 gL^{-1} in the same medium. This test is similar to the grinding tests as regards the concentration of the suspension. After 3 h of testing in coupled mode, 63% of the cerium is dissolved.

The grinding having already been optimized and not allowing to exceed the 63% dissolved in 3 h, it is the attack conditions which have been modified. Other tests were carried out for different acidities: 4 M and 8.5 M, thus making it possible to reach 86% of solubilized cerium.

The analysis of the kinetics and the structural effects of grinding on the material led to the understanding of the phenomena during the grinding / dissolution coupling. Unlike the decoupled process, the simultaneous grinding and dissolution of CeO_2 is not limited to the dissolution of the activated part of the solid which no longer exhibits structural modifications beyond one hour of grinding. The size of the particles in a process combining grinding and dissolution continues to decrease, even after 1 h. After 1 hour, grinding (in water) reduces the size of the particles down to the nanometric scale (appearance of Ce^{3+}) and generates the creation of structural defects (dislocations). The XRD analysis of a coupling residue at 1 h demonstrates the characteristic mechanism and makes it possible to understand how the dissolution of the ground material is governed. During the grinding / dissolution coupling, just as with a simple grinding, the particles will gradually decrease both thanks to the grinding but also under the effect of the dissolution. This dissolution is accelerated after 40 min by the formation and simultaneous dissolution of the smallest nanoparticles (less than 40 nm) having a reduced layer of Ce^{3+} on the surface.

Thus, the dissolution of the reference material within the framework of a decoupled process composed of a first regime is characterized by the dissolution of the Ce^{3+}- based nanoparticles. The second regime corresponds to the dissolution of the particles containing the dislocations.

Finally, the temperature is the parameter that has been identified to greatly improve the dissolution kinetics, it will be studied as a perspective following this thesis project to achieve a dissolution rate of 100% for an operating time of less. from 3h.

This project has received funding from the EURATOM research and training programme 2017-2021 under grant agreement No 755171. The content of this deliverable reflects only the author's view. The European Commission is not responsible for any use that may be made of the information it contains.

CONCLUSION

The use of the Micro Series mill, made it possible through different stress modes applied to the sample to reduce the size of the reference CeO_2 particles down to the nanometer scale. This reduction in particle size results, in a first approach, by an increase in the specific surface from 0.7 to 29.5 $m^2.g^{-1}$. The combination of particle size data and microscopic observations led to the conclusion of a two-stage grinding mechanism. From the first moments, the impacts of the balls weaken the grain boundaries present in the platelets. As the grinding progresses, when the size decreases, the grinding mechanism becomes transgranular, thus leading after 1 h of grinding to two populations of particles. A first population consists of grains of the order of a micrometer and with defects that have been identified as dislocations. They can both pass through crystallites, making them easier to rupture and decrease the size of coherent domains, or accumulate near a point of impact causing an increase in internal energy in the crystallite. The second population corresponds to nanoparticles. Their analysis by transmission electron microscopy and EELS indicates a core-shell effect as a function of size, with cerium on the surface at oxidation degree + III. It appears that for sizes less than 5 nm the particles are exclusively composed of Ce^{+3}.

Dissolution tests ($[HNO_3]$ = 8.5 M and T = 95 ° C) of the reference sample after grinding demonstrate a significant increase in dissolution kinetics. This increase in dissolution rates at 6 h by a factor of 360 is partly explained by an increase in specific surface area. If this is the majority effect with an increase by a factor of 120, one or more other phenomenon (s) brought about by grinding increases the dissolution kinetics. It also appears a change in the mechanisms with the observation of a kinetics in two regimes on the crushed samples against only one on the unground samples. The analysis of the Ziouane kinetic model made it possible by analogy to identify that the second regime is governed by the dissolution of particles containing dislocations reducing the size of the coherent domains. Thus, the first regime of the dissolution of the reference material within the framework of a decoupled process is characterized by the dissolution of the nanoparticles containing Ce^{3+}. The second regime corresponds to the dissolution of the particles containing the dislocations.

The modification of certain grinding parameters made it possible to maximize the first, faster dissolution rate. The grinding time made it possible in particular to realize that beyond 60 min the additional effects generated by the grinding on the solid are negligible, resulting in dissolution rates which do not exceed 41% after 6 h . The limits of the grinding and then dissolution process having been reached, the coupling process therefore appears as the solution to keep the activation of the solid until it is completely dissolved.

The simultaneous grinding / dissolution tests on CeO_2 under mild chemical attack conditions ($[HNO_3]$ = 0.5 M and T = 50 ° C) led after 3 h to a dissolution rate of 33% much higher than 0.5% achieved with simple grinding (at 6 h of dissolution). To increase the dissolution rate, the concentration of the suspension was reduced and, after 3 hours of testing in coupled mode, it was possible to reach 63% of dissolved cerium. The attack conditions were then changed. Further tests were carried out for different acidities: 4 M and 8.5 M, thus making it possible to reach 86% of solubilized cerium in three hours. Unlike the decoupled process, the simultaneous grinding and dissolution of CeO_2 is not limited. During the grinding / dissolution coupling, the particle size gradually decreases both thanks to grinding but also under the effect of dissolution. This dissolution is accelerated after 40 min by the formation and simultaneous dissolution of the smallest nanoparticles (less than 40 nm) having a reduced layer of Ce^{3+} on the surface.

This project has received funding from the EURATOM research and training programme 2014-2018 under grant agreement No 755171. The content of this deliverable reflects only the author's view. The European Commission is not responsible for any use that may be made of the information it contains.

REFERENCES

[1] Touron, E., Boullis, B., Chabert, C., 2016. Overview of fuel cycle perspective for France.

[2] D. Vollath, H. Wedemeyer, H. Elbel, E. Günther, On the Dissolution of (U,Pu)O2 Solid Solutions with Different Plutonium Contents in Boiling Nitric Acid, Nucl. Technol. 71 (1985) 240–245. https://doi.org/10.13182/NT85-A33723.

[3] Brueziere, J., Tribout-Maurizi, A., Durand, L., Bertrand, N., 2013. Polyvalent fuel treatment facility (TCP): shearing and dissolution of used fuel at La Hague facility. American Nuclear Society - ANS; La Grange Park (United States).

[4] J.H. Goode, HOT-CELL DISSOLUTION OF HIGHLY IRRADIATED 20% PuO $ sub 2$-80% UO $ sub 2$ FAST-REACTOR FUEL SPECIMENS, Oak Ridge National Lab., Tenn., 1965.

[5] A.L. Uriarte, R.H. Rainey, Dissolution of High-Density UO2, PuO2 and UO2-PuO2 Pellets in Inorganic Acids, 1965.

[6] S. Fournier, Etude de la dissolution des oxydes mixtes (U,Pu)O2 à forte teneur en plutonium, thesis, Montpellier 2, 2000. http://www.theses.fr/2000MON20203 (accessed May 18, 2020).

[7] Katz, J.J., Seaborg, G.T., Morss, L.R., 1987. Chemistry of the actinide elements. Second edition.

[8] G. Scott Barney, The kinetics of plutonium oxide dissolution in nitric/hydrofluoric acid mixtures, J. Inorg. Nucl. Chem. 39 (1977) 1665–1669. https://doi.org/10.1016/0022-1902(77)80123-1.

[9] Bourges, J., Madic, C., Koehly, G., Lecomte, M., 1986. Dissolution of plutonium dioxide in nitric acid media by silver(II) electroreduction. J. -Common Met. 122 pp. 303–311.

[10] A.E. Blum, R.A. Yund, A.C. Lasaga, The effect of dislocation density on the dissolution rate of quartz, Geochim. Cosmochim. Acta. 54 (1990) 283–297. https://doi.org/10.1016/0016-7037(90)90318-F.

[11] Corkhill, C.L., Myllykylä, E., Bailey, D.J., Thornber, S.M., Qi, J., Maldonado, P., Stennett, M.C., Hamilton, A., Hyatt, N.C., 2014. Contribution of Energetically Reactive Surface Features to the Dissolution of CeO 2 and ThO 2 Analogues for Spent Nuclear Fuel Microstructures. ACS Appl. Mater. Interfaces 6, 12279–12289. https://doi.org/10.1021/am5018978.

[12] D. Tromans, J.A. Meech, Enhanced dissolution of minerals: stored energy, amorphism and mechanical activation, Miner. Eng. 14 (2001) 1359–1377. https://doi.org/10.1016/S0892-6875(01)00151-0.

[13] Claparede, L., Tocino, F., Szenknect, S., Mesbah, A., Clavier, N., Moisy, P., Dacheux, N., 2015. Dissolution of Th1−xUxO2: Effects of chemical composition and microstructure. J. Nucl. Mater. 457, 304–316. https://doi.org/10.1016/j.jnucmat.2014.11.094

[14] N.F. Albanese-Kotar, D.E. Mikkola, Dissolution of comminuted magnesium oxide as affected by the density of dislocations introduced by various comminution methods, Mater. Sci. Eng. 91 (1987) 233–240. https://doi.org/10.1016/0025-5416(87)90302-8.

[15] P. Baláž, J. Ficeriová, V. Šepelák, R. Kammel, Thiourea leaching of silver from mechanically activated tetrahedrite, Hydrometallurgy. 43 (1996) 367–377. https://doi.org/10.1016/0304-386X(96)00015-1.

[16] A. Blum, A. Lasaga, Role of surface speciation in the low-temperature dissolution of minerals, Nature. 331 (1988) 431–433.

[17] K. Tkáčová, P. Baláž, B. Mišura, V.E. Vigdergauz, V.A. Chanturiya, Selective leaching of zinc from mechanically activated complex Cu・Pb・Zn concentrate, Hydrometallurgy. 33 (1993) 291–300. https://doi.org/10.1016/0304-386X(93)90068-O.

[18] Ziouane, Y., Milhau, T., Maubert, M., Arab-Chapelet, B., Leturcq, G., 2018. Dissolution kinetics of CeO2 powders with different morphologies and analogy to PuO2 dissolution. Hydrometallurgy 177, 205–213. https://doi.org/10.1016/j.hydromet.2018.03.016

[19] C.L. Corkhill, D.J. Bailey, F.Y. Tocino, M.C. Stennett, J.A. Miller, J.L. Provis, K.P. Travis, N.C. Hyatt, Role of Microstructure and Surface Defects on the Dissolution Kinetics of CeO 2 , a UO 2 Fuel Analogue, ACS Appl. Mater. Interfaces. 8 (2016) 10562–10571. https://doi.org/10.1021/acsami.5b11323.

[20] D. Horlait, N. Clavier, S. Szenknect, N. Dacheux, V. Dubois, Dissolution of Cerium(IV)–Lanthanide(III) Oxides: Comparative Effect of Chemical Composition, Temperature, and Acidity, Inorg. Chem. 51 (2012) 3868–3878. https://doi.org/10.1021/ic300071c.

This project has received funding from the EURATOM research and training programme 2014-2018 under grant agreement No 755171. The content of this deliverable reflects only the author's view. The European Commission is not responsible for any use that may be made of the information it contains.

[21] Horlait, D., Claparede, L., Tocino, F., Clavier, N., Ravaux, J., Szenknect, S., Podor, R., Dacheux, N., 2014. Environmental SEM monitoring of Ce1−xLnxO2−x/2 mixed-oxide microstructural evolution during dissolution. J. Mater. Chem. A 2, 5193–5203. https://doi.org/10.1039/C3TA14623E

[22] X. Beaudoux, M. Virot, T. Chave, G. Durand, G. Leturcq, S.I. Nikitenko, Vitamin C boosts ceria-based catalyst recycling, Green Chem. 18 (2016) 3656–3668. https://doi.org/10.1039/C6GC00434B.

[23] L. Joret, Influence d'un rayonnement microonde sur la cinetique de dissolution de uo2, ceo2 et co3o4 en milieu nitrique, thesis, Paris 6, 1995. http://www.theses.fr/1995PA066117 (accessed April 29, 2019).

[24] Dalodière, E., Virot, M., Morosini, V. et al., 2017 Insights into the sonochemical synthesis and properties of salt-free intrinsic plutonium colloids. Sci Rep 7, 43514. https://doi.org/10.1038/srep43514.

[25] Beaudoux, X., Virot, M., Chave, T., G., Leturcq, G., Jouan G., Venault L., Moisy P. and Nikitenko, S.I., 2016b. Ultrasound-assisted reductive dissolution of CeO2 and PuO2 in the presence of Ti particles. Dalton Trans., 2016, 45, 8802. https://doi.org/10.1039/c5dt04931h.

[26] Burney, G.A., Smith, P.K., 1984. Controlled PuO/sub 2/particle size from Pu (III) oxalate precipitation. Du Pont de Nemours (EI) and Co., Aiken, SC (USA). Savannah River Lab.

[27] Rankin, D.T., Burney, G.A., 1975. Particle size of 238-Pu02 obtained by oxalate precipitation and calcination. Bull. Amer. Ceram. Soc 54, 1061–1065.

[28] Agarwala, K.P., Naik, M.C., 1961. Kinetics of decomposition of yttrium, cerous and zirconyl oxalates. Anal. Chim. Acta 24, 128–133. https://doi.org/10.1016/0003-2670(61)80027-5

[29] De Almeida, L., Grandjean, S., Vigier, N., Patisson, F., 2012. Insights into the thermal decomposition of lanthanide (III) and actinide (III) oxalates–from neodymium and cerium to plutonium. Eur. J. Inorg. Chem. 2012, 4986–4999.

[30] J. Heintz, J. Bernier, SYNTHESIS AND SINTERING PROPERTIES OF CERIUM OXIDE POWDERS PREPARED FROM OXALATE PRECUSORS, J. Phys. Colloq. 47 (1986) C1-25-C1-29. https://doi.org/10.1051/jphyscol:1986104.

[31] M. Leblanc, G. Leturcq, E. Welcomme, X. Deschanels, T. Delahaye, Actinide mixed oxide conversion by advanced thermal denitration route, J. Nucl. Mater. 519 (2019) 157–165. https://doi.org/10.1016/j.jnucmat.2019.03.049.

[32] Petříček, V., Dušek, M., Palatinus, L., 2014. Crystallographic Computing System JANA2006: General features. Z. Für Krist. - Cryst. Mater. 229, 345–352. https://doi.org/10.1515/zkri-2014-1737.

[33] L. Claparede, N. Clavier, N. Dacheux, A. Mesbah, J. Martinez, S. Szenknect, P. Moisy, Multiparametric Dissolution of Thorium–Cerium Dioxide Solid Solutions, Inorg. Chem. 50 (2011) 11702–11714. https://doi.org/10.1021/ic201699t.

[34] Hailstone, R.K., DiFrancesco, A.G., Leong, J.G., Allston, T.D., Reed, K.J., 2009. A Study of Lattice Expansion in CeO2 Nanoparticles by Transmission Electron Microscopy. J. Phys. Chem. C 113, 15155–15159. https://doi.org/10.1021/jp903468m.

[35] Younis, A., Chu, D., Li, S., 2016. Cerium Oxide Nanostructures and their Applications. Funct. Nanomater. https://doi.org/10.5772/65937.

[36] F. Zhang, Q. Jin, S.-W. Chan, Ceria nanoparticles: Size, size distribution, and shape, J. Appl. Phys. 95 (2004) 4319–4326. https://doi.org/10.1063/1.1667251

[37] R. Ma, M. Jahurul Islam, D. Amaranatha Reddy, T.K. Kim, Transformation of CeO2 into a mixed phase CeO2/Ce2O3 nanohybrid by liquid phase pulsed laser ablation for enhanced photocatalytic activity through Z-scheme pattern, Ceram. Int. 42 (2016) 18495–18502. https://doi.org/10.1016/j.ceramint.2016.08.186.

[38] M.C. Spadaro, P. Luches, G. Bertoni, V. Grillo, S. Turner, G. Van Tendeloo, S. Valeri, S. D'Addato, Influence of defect distribution on the reducibility of CeO_{2-x} nanoparticles, Nanotechnology. 27 (2016) 425705. https://doi.org/10.1088/0957-4484/27/42/425705.

[39] S. Turner, S. Lazar, B. Freitag, R. Egoavil, J. Verbeeck, S. Put, Y. Strauven, G. Van Tendeloo, High resolution mapping of surface reduction in ceria nanoparticles, Nanoscale. 3 (2011) 3385. https://doi.org/10.1039/c1nr10510h.

This project has received funding from the EURATOM research and training programme 2014-2018 under grant agreement No 755171. The content of this deliverable reflects only the author's view. The European Commission is not responsible for any use that may be made of the information it contains.

[40] L. Claparede, N. Clavier, N. Dacheux, P. Moisy, R. Podor, J. Ravaux, Influence of Crystallization State and Microstructure on the Chemical Durability of Cerium–Neodymium Mixed Oxides, Inorg. Chem. 50 (2011) 9059–9072. https://doi.org/10.1021/ic201269c.

[41] A.A. Benzerga, Y. Bréchet, A. Needleman, E. Van der Giessen, The stored energy of cold work: Predictions from discrete dislocation plasticity, Acta Mater. 53 (2005) 4765–4779. https://doi.org/10.1016/j.actamat.2005.07.011.

[42] A.E. Blum, R.A. Yund, A.C. Lasaga, The effect of dislocation density on the dissolution rate of quartz, Geochim. Cosmochim. Acta. 54 (1990) 283–297. https://doi.org/10.1016/0016-7037(90)90318-F.

[43] R. Gers, E. Climent, D. Legendre, D. Anne-Archard, C. Frances, Numerical modelling of grinding in a stirred media mill: Hydrodynamics and collision characteristics, Chem. Eng. Sci. 65 (2010) 2052–2064. https://doi.org/10.1016/j.ces.2009.12.003.

[44] S. Ouattara, Nanobroyage d'actifs organiques en suspensions concentrées dans un broyeur à billes agité., Institut National Polytechnique de Toulouse, 2010.

[45] C. Varinot, H. Berthiaux, J. Dodds, Prediction of the product size distribution in associations of stirred bead mills, Powder Technol. 105 (n.d.) 228–236.

[46] H. Bel Fadhel, C. Frances, Wet batch grinding of alumina hydrate in a stirred bead mill, Powder Technol. 119 (2001) 257–268. https://doi.org/10.1016/S0032-5910(01)00266-2.

[47] F. Garcia, Élaboration de suspensions microniques de carbonate de calcium à propriétés contrôlées par broyage en voie humide, These de doctorat, Toulouse, INPT, 2001. https://www.theses.fr/2001INPT025G (accessed January 25, 2021).

[48] E. Dalodière, Sonochimie du plutonium : synthèse et spéciation en solution et à l'état colloïdal, thesis, Montpellier, 2017. http://www.theses.fr/2017MONTT177 (accessed April 29, 2019).

[49] L. Takacs, J.S. McHenry, Temperature of the milling balls in shaker and planetary mills, J. Mater. Sci. 41 (2006) 5246–5249. https://doi.org/10.1007/s10853-006-0312-4.

[50] R. Verma, S.K. Samdarshi, S. Bojja, S. Paul, B. Choudhury, A novel thermophotocatalyst of mixed-phase cerium oxide (CeO2/Ce2O3) homocomposite nanostructure: Role of interface and oxygen vacancies, Sol. Energy Mater. Sol. Cells. 141 (2015) 414–422. https://doi.org/10.1016/j.solmat.2015.06.027.

ANNEXES

This project has received funding from the EURATOM research and training programme 2014-2018 under grant agreement No 755171. The content of this deliverable reflects only the author's view. The European Commission is not responsible for any use that may be made of the information it contains.